Terahertz Surface Plasmon Polariton-like Surface Waves for Sensing Applications

by

Amir Arbabi

A thesis
presented to the University of Waterloo
in fulfillment of the
thesis requirement for the degree of
Master of Applied Science
in
Electrical and Computer Engineering

Waterloo, Ontario, Canada, 2009

I hereby declare that I am the sole author of this thesis. This is a true copy of the thesis, including any required final revisions, as accepted by my examiners.

I understand that my thesis may be made electronically available to the public.

Abstract

Surface plasmon polaritons are electromagnetic surface waves coupled to electron plasma oscillation of metals at a metal-dielectric interface. At optical frequencies, these modes are of great interest because of their high confinement to a metal-dielectric interface. Due to the field enhancement at the interface, they have been used in different applications such as sensors, second harmonic generation and enhanced Raman scattering. Surface plasmon resonance based sensors are being used for detection of molecular adsorption such as DNA and proteins. These sensors are known to be highly sensitive and have successfully become commercialized.

Terahertz (THz) frequency band of electromagnetic spectrum has attracted researchers in the last few years mostly because of sensing and imaging applications. Many important chemical and biological molecules have their vibrational and rotational resonance frequencies in the THz range that makes the THz sensing one of the most important applications of THz technology.

Considering above mentioned facts, extending the concept of surface plasmon sensors to THz frequencies can result in sensitive sensors. In this work the possibility of this extension has been investigated. After reviewing optical surface plasmon polariton waves and a basic sensor configuration, surface plasmon polariton waves propagating on flat metallic and doped semiconductor surfaces have been examined for this purpose. It has been shown that these waves on metallic surfaces are loosely confined to the metal-dielectric interface and doped semiconductors are also too lossy and cannot meet the requirements for sensing applications.

Afterwards, it is shown that periodically patterned metallic surfaces can guide surface waves that resemble surface plasmon polariton waves. A periodically patterned metallic surface is used to guide THz surface plasmon polariton-like surface waves and a highly sensitive sensor is proposed based on that. The quasi-optical continuous wave (CW) THz radiation is coupled to this structure using the Otto's attenuated total reflection (ATR) configuration and the sensitivity of the device is discussed.

A general scattering parameter based model for prism coupling has been proposed and verified. It is shown that a critical coupling condition can happen by changing the gap size between the prim and periodic surface. Details of fabrication of the periodic structure and experimental setup have also been presented.

Acknowledgements

I would like to thank god for showering all his blessings upon me whenever I needed and more than I had asked for. I would like to express the deepest and warmest gratitude to my parents and my brother for their unconditional love, self-sacrifice and support through my life.

I wish to thank my supervisor Professor Safavi-Naeini for his guidance, kindness and support. I am grateful of him for his insightful discussions and comments about my work. Without his guidance, preparing this thesis would have been impossible. Especial thanks to Dr. Rohani for collaborating in this work. I also appreciate Dr. Saeedkia and Mr. Neshat for their help and valuable discussions we had during my research.

I would like to also express my sincere gratitude to my seminar committee members, Professor Majedi and Professor Saini for their time, careful reading, and helpful comments. Last but not least, I would like to express my appreciation to my friends Javad, Mohammad and Payam.

Dedication

To my Parents
for their never ending love

Contents

List of Figures

Chapter 1

Introduction

1.1 Motivation and Objectives

Fundamental research and development of surface plasmon polariton based structures and devices have attracted several researchers in recent years. Surface plasmon polaritons are collective oscillations of electrons coupled to electromagnetic field that occur at an interface between a conductor and a dielectric. They can take various forms, ranging from freely propagating electron density waves along metal surfaces to localized electron oscillations on metallic nanoparticles. Their unique properties enable a wide range of practical applications including light guiding and manipulation at nanoscale, biodetection at single molecule level, enhanced optical transmission through subwavelength apertures, and high resolution optical imaging below the diffraction limit. One of the most successful applications of surface plasmon polaritons at optical frequencies has been surface plasmon polariton resonance based sensors. These sensors are well known for their high sensitivity, have been commercialized, and are being used for bio-sensing applications.

Although surface plasmon polaritons have been known in the optical region for more than a century, their investigation in the THz band is limited to last few years. With the development of short-pulse lasers, THz spectroscopy has opened up an interesting but hardly accessible spectral window where a large variety of gases, liquids, and solids show specific resonances. THz applications range from studies of coherent excitations in semiconductor heterostructures to medical diagnostics and three dimensional imaging systems for monitoring industrial processes. Many important chemical and biological molecules have their vibrational and rotational resonance frequencies in the THz range and this fact makes the THz sensing one of the most important applications in THz technology.

Considering the success of surface plasmon polariton based sensors at optical frequencies and the demand for highly sensitive sensors at THz frequencies, practical applications for THz surface plasmon polariton based sensors can be expected. The main purpose of this thesis is to extend the idea of surface plasmon polariton based sensors to THz frequencies. Although a simple layer of metal supports strongly confined surface plasmon polaritons at optical frequencies, at THz frequencies metals resemble in many ways a perfect electric conductor and the negligible penetration of the electromagnetic fields into them leads to highly delocalized surface plasmon polaritons. For sensing purposes, strongly localized field is essential and can be achieved by using engineered materials that guide strongly confined surface plasmon polariton-liked surface waves.

1.2 Literature Review

Optical surface plasmon polaritons are investigated widely in literature. Excellent introduction to the optical surface plasmon polaritons can be found in various books [7, 13] and numerous papers [8, 2]. The pioneer experimental setup was discussed in the classic work of Otto [19], and Kretschmann and Raether [10].

THz surface plasmon polaritons have also been used for guiding of THz waves outside of a bare metallic cylinder [22]. Applications of surface waves propagating on a metallic periodic structure have been discussed in [20]. In [20] a simple approximate method has been used to find effective material parameter for the case where the period of the structure is much smaller than the wavelength of the waves. The method had previously been used in [5] and [3]. Existence of these kind of surface waves at microwave frequencies have been reported in [6] and [11]. [11] is a recent article that has used the Otto's coupling configuration for coupling of waves to the periodic structure.

At THz frequencies, [12] has used a corrugated wire for guiding and focusing of surface waves propagating on the wire's surface and [14] has proposed a THz sensor which works based on the spectrum of a THz pulse that has been transmitted through a metallic surface which is perforated periodically in two dimensions. Recently, guiding of THz pulsed waves on a periodic metallic structure made of an array of holes has been reported [23]. For coupling of a THz beam to surface waves, a sharp razor blade has been used which diffracts the incident waves and some of it is being coupled to surface waves. Finally, it should be noted that some parts of the research work demonstrated in this thesis have been presented in [1].

1.3 Thesis Overview

Following this chapter, chapter 2 will be begun by an introduction to optical surface plasmon polaritons propagating on a metal-dielectric interface. After investigating metal's optical properties and reviewing the Drude model, methods for excitations of these waves will be presented. THz surface plasmon polaritons that propagate on a metal surface are discussed afterwords, it has been shown that these waves are loosely bonded to the metal-dielectric interface, and are not suitable for sensing applications.

Surface waves which propagate on the surface of a periodically patterned metal and have field distribution similar to that of surface plasmon polaritons are investigated in chapter 3. A periodic metallic structure is proposed. Simulation method and an ATR coupling configuration are demonstrated and it is shown that this configuration can be used as a highly sensitive sensor. A sensitivity parameter has been defined and is related to the group delay of the surface wave.

A novel method for analyzing prism coupling to periodic structures is introduced in chapter 4. The method is based on scattering parameter model for each cell of the structure. The validity of the method is investigated by using full wave EM simulations. Using the introduced method, coupling of a Gaussian beam to the structure is simulated.

Details of fabrication and characterization of the device proposed in chapter 3 have been presented in chapter 5. An experimental setup designed for coupling of a THz beam to surface waves propagating on the fabricated structure has also been explained in this chapter. The last chapter summarizes the thesis and proposes future research in this area.

Chapter 2

Optical and Terahertz Surface Plasmon Polaritons

2.1 Surface Plasmon Polaritons at Optical Frequencies

An overview of optical surface plasmon polaritons is presented in this chapter. The optical properties of metals are reviewed and optical surface plasmon polariton waves that propagate along a metal-dielectric interface are studied. Following this analysis, the possibility of existence of surface plasmon polariton mode at THz frequencies at metal-dielectric and semiconductor-dielectric interfaces are discussed. It is shown that although these structures support THz surface plasmon polaritons, these waves are not strongly confined to the structure or are excessively lossy and cannot be used for sensing applications.

2.1.1 Metals at optical frequencies

Metals show large imaginary and negative real permittivity at microwave frequencies and can be approximated as a Perfect Electric Conductor (PEC) at these frequencies. As the frequency increases, the free electrons of metals can not respond to the electric field spontaneously and show a dynamic response to the excitation. The retardation made by this dynamic response, causes a phase difference between the electric field $\overrightarrow{E}$ and the current density $\overrightarrow{J}$.

Over a wide frequency range, the optical properties of metals can be explained by a free electron model, where a gas of free electrons of number density n moves against a fixed background of positive ion cores. This model is also known as the Drude model. In the plasma model, details of the lattice potential and electron-electron interactions are not taken into account. Instead, one simply assumes that some aspects of the band structure are incorporated into the effective optical mass m of each electron. The electrons oscillate in response to the applied electromagnetic field, and their motion is damped via collisions occurring with a characteristic collision frequency $\omega_t = \frac{1}{\tau}$ where τ is known as the relaxation time of the free electron gas.

Using a simple second order differential equation of motion for an electron in the plasma sea, the conductance and consequently the complex permittivity for metals can be found as:

$$\epsilon_r(\omega) = \epsilon_\infty - \frac{\omega_p^2}{\omega(\omega - j\omega_t)} \tag{2.1}$$

where ϵ_∞ is the high frequency dielectric constant of metal and

$$\omega_p = \sqrt{\frac{n}{\epsilon_0 m}}e \tag{2.2}$$

is the plasma frequency of free electron gas. For large frequencies close to ω_p, the product $\omega\tau \gg 1$, leading to negligible damping. Here, $\epsilon(\omega)$ is predominantly real, and

$$\epsilon_r(\omega) = \epsilon_\infty - \frac{\omega_p^2}{\omega^2} \tag{2.3}$$

can be taken as the dielectric function of the undamped free electron plasma. ϵ_∞ is close to unity for most of the metals of interest. As this equation shows the permittivity of metals is negative at frequencies smaller than plasma frequency. It should also be noted that the behavior of noble metals in the optical frequency region is altered by interband transitions, leading to an increase in imaginary part of the permittivity [7].

2.1.2 Surface plasmon polaritons on metal-dielectric interface

As it was mentioned in the previous section, real part of permittivity of some metals are negative at optical frequencies. In this section it is shown that this negative permittivity

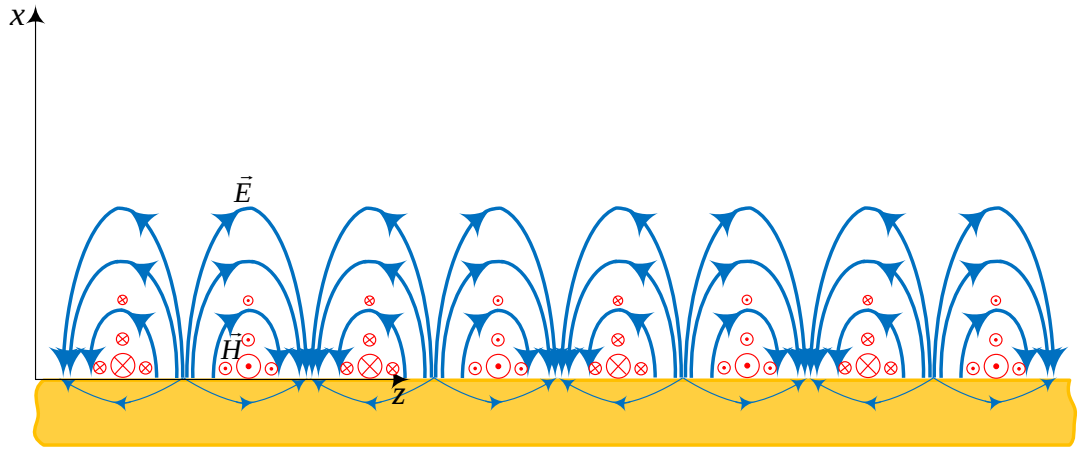

Figure 2.1: Electric and magnetic fields of surface plsmon polariton mode propagating in the $\hat{z}$ direction.

of metals leads to existence of a kind of surface waves which propagates along a metal-dielectric boundary and are referred to as surface plasmon polaritons.

Consider a waveguide consisting of a semi-infinite metal with complex permittivity of $\epsilon_m = \epsilon'_m - j\epsilon''_m$, and a semi-infinite dielectric with permittivity of ϵ_d as shown in Fig. 2.1. The propagation constants of guided modes propagating along such a structure and are independent of y can be calculated by writing the possible solutions of the Maxwell's equations for surface waves in each region and applying boundary conditions. The dispersion equation will be found to be [7]:

$$\gamma_m = -\gamma_d \quad \text{for TE modes,} \tag{2.4}$$

$$\frac{\gamma_m}{\epsilon_m} = -\frac{\gamma_d}{\epsilon_d} \quad \text{for TM modes} \tag{2.5}$$

where $\gamma_i^2 = k_z^2 - k_i^2$. For having a surface wave, we need both γ_m and γ_d to have a positive real part, thus according to (2.4) TE surface plasmon modes cannot exist in this structure. In contrast, because of different signs of the permittivity of metal and dielectric, TM modes (2.5) can be guided in this structure and the propagation constant can be calculated from (2.5) to be:

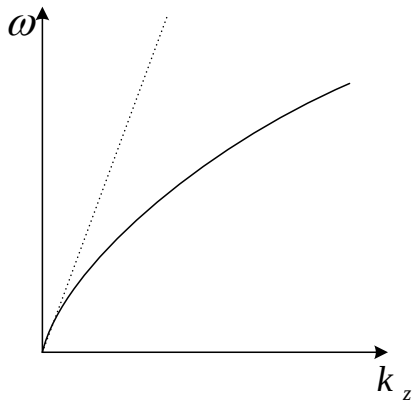

Figure 2.2: A nominal surface plasmon dispersion relation. The dotted line shows the free space dispersion relation.

$$k_z^{SP} = k_0 \sqrt{\frac{\epsilon_m \epsilon_d}{\epsilon_m + \epsilon_d}} = k_z' - j k_z'' \tag{2.6}$$

In (2.6), k_z' is the phase constant and k_z'' is the extinction constant of the surface plasmon polariton mode. Propagation length of this mode is define as $L = \frac{1}{2k_z''}$ which represents the distance in the direction of propagation at which the energy of the surface plasmon polariton decreases by a factor of $\frac{1}{e}$. The propagation length is in the order of few micrometers for noble metals in the visible range of the optical spectrum. A nominal dispersion relation for a noble metal with air as a dielectric, and the free space dispersion relation are depicted in Fig. 2.2. As this figure shows, the propagation constant for the surface plasmon polariton mode is always larger than that of a propagating plane wave, therefore, these modes cannot be excited by illuminating the structure by a propagating light wave and other methods of excitation must be used.

The electric and magnetic fields for these modes are shown in Fig. 2.1. As can be seen in this figure, fields are confined to the surface and decreases exponentially in the dielectric and metal. Strong confinement of fields is the most important property of surface plasmon polaritons which leads to large field amplitude at the interface which is essential in many different applications such as biomedical sensors and enhanced nonlinear phenomena at the interface.

Penetration depth of fields into dielectric and metal are defined as $L_d = \frac{1}{2\mathrm{Re}(\gamma_d)}$ and $L_m = \frac{1}{2\mathrm{Re}(\gamma_m)}$. In the visible range, L_m is in the order of ten nanometer and L_d is in the

order of hundreds of nanometers for Gold, Silver and Aluminum. Therefore, the fields are localized to a region above the metal-dielectric boundary which is about $\frac{\lambda}{5}$ thick. The field confinement to the surface in the dielectric side decreases as the wavelength increases and the field will be less confined to the surface.

2.1.3 Physical nature of surface plasmon polaritons

Considering the above results, it can concluded that surface plasmon polaritons are surface waves that propagate along the surface of a conductor, usually a metal. These waves are essentially light waves that are trapped on the surface because of their interaction with the free electrons of the conductor. In this interaction, the free electrons respond collectively by oscillating in resonance with the light wave. The resonant interaction between the surface charge oscillation and the electromagnetic field of the light constitutes the surface plasmon polariton and gives rise to its unique properties.

2.1.4 Excitation of surface plasmon polaritons

As it was mentioned in the previous section, phase constant of a surface plasmon polariton mode is larger than the propagation constant in a dielectric medium above the metallic surface and this mode cannot be excited by illuminating a light beam on the metal-dielectric interface.

There are three common methods for exciting surface plasmon polaritons by light. The most common approach of excitation of these waves is by means of a prism coupler and the Attenuated Total Reflection (ATR) method. In this method surface plasmon polaritons are excited by the evanescent field of the totally reflected wave in a prism coupler (Figs. 2.3 and 2.4). In the Fig. 2.3 (known as the Otto configuration) the prism is on the dielectric side and the evanescent filed of the prim couples to the surface plasmon polariton mode, while in the Fig. 2.4, which is refereed to as the Kretschmann configuration, the evanescent fields after passing through a thin metal layer, excites the surface plasmon polariton mode on the other side of the metal surface. The first structure does not need a nanometer thick metal layer, but requires accurate adjustment of the prism above the metal. In these structures, the light will be coupled to the surface plasmon polariton mode when its phase constant becomes equal to the phase constant of the surface plasmon polariton mode, that is:

$$k_z^{SP} = n_p k_0 \sin(\theta) \tag{2.7}$$

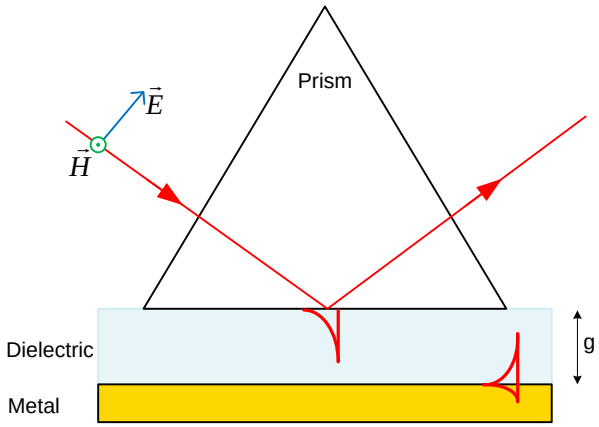

Figure 2.3: Otto's ATR configuration for coupling of waves into surface plasmon polariton mode.

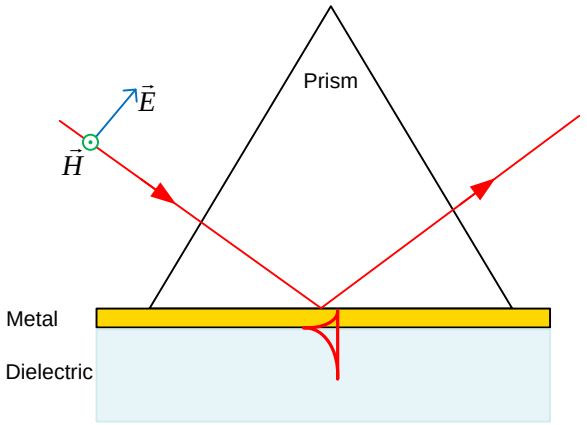

Figure 2.4: Kretschmann's ATR configuration for coupling of waves into surface plasmon polariton mode.

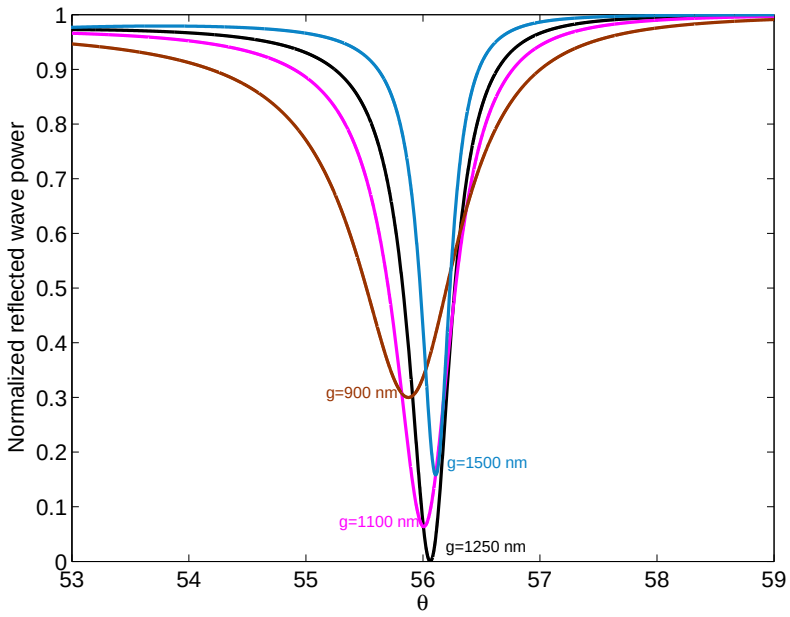

Figure 2.5: Normalized power of a reflected plane wave for different values of gap size g in the Otto's configuration (Figs. 2.3). The metal is assumed to be Gold with $\epsilon_m = -25 - j1.44$ at the wavelength of $\lambda_0 = 800nm$, the dielectric above the Gold's surface is air with $\epsilon_d = 1$ and the refractive index of the prism is assumed to be $n_p = 1.51$ (BK7 glass).

When the light is coupled to the surface plasmon polariton mode, the reflected wave will become small. Figs. 2.5 shows the normalized power of a reflected plane wave as a function of the incident angle θ for different values of gap size g in the Otto's configuration (Figs. 2.3). The metal is assumed to be Gold with $\epsilon_m = -25 - j1.44$ at the wavelength of $\lambda_0 = 800nm$, the dielectric above the Gold's surface is air with $\epsilon_d = 1$ and the refractive index of the prism is assumed to be $n_p = 1.51$ (BK7 glass). It can be deduced from this figure that there is an optimum value for g which minimizes the reflected wave at the coupling angle. This angle is sensitive to the permittivity of the dielectric medium near the surface of the metal and can be used to measure refractive index of a sample with high accuracy.

In the second method, the coupling of energy to the surface plasmon polaritons is performed by using a diffraction grating. When the light beam impinges a grating, different orders of diffraction will be created and the surface plasmon polariton modes will be excited

if one of these orders of diffraction has the same phase constant as the surface plasmon polariton mode,

$$k_z^{SP} = k_z + \frac{m}{2\pi\Gamma} \tag{2.8}$$

where Γ is the period of the grating.

The third approach for excitation of surface plasmon polaritons is using the evanescent wave of a dielectric waveguide. In this approach the coupling happens when the phase constant of the dielectric waveguide mode becomes equal to the that of surface plasmon polaritons and this can be achieved by changing the frequency of the guided light.

2.2 Surface Plasmon Polaritons at Terahertz Frequencies

In this section the possibility of exciting surface plasmon waves and their properties at THz frequencies is discussed. At first, the permittivity of metals at this frequency band is presented and it is shown that surface plasmon polaritons propagating on a flat metallic surface are weakly bonded to the metallic surface. At the end other candidates such as doped semiconductors and structured metal surfaces have been examined.

2.2.1 Terahertz surface plasmons on a dielectric-metal interface

The difference between THz and optical surface plasmon polaritons stems from different permittivities of metals at these two frequency bands. As it was stated in the previous chapter, the electromagnetic behavior of many metals at frequencies smaller than their plasma frequencies, can be well described by free electron model. Equation (2.1), can be almost accurately fitted to the experimentally measured permittivity values of many metals in a wide range of frequencies including terahertz band [18, 17, 15, 16]. Recalling (2.1):

$$\epsilon_r(\omega) = \epsilon_\infty - \frac{\omega_p^2}{\omega(\omega - j\omega_t)} \tag{2.9}$$

$\epsilon_\infty = 1$ for most of metals and value of plasma and collision frequencies of some metals are being provided in Table 2.1 [17]. As can be seen, the plasma frequency for all of these metals fall in the visible and ultraviolet part of the spectrum. This result in large

Table 2.1: Plasma and collision frequencies of some metals [17].

Metal	f_p [THz]	f_t [THz]
Al	3570	19.80
Co	960	8.85
Cu	1788	2.20
Au	2184	6.45
Fe	990	4.41
Pb	1782	48.90
Mo	1806	12.36
Ni	1182	10.56
Pd	1320	3.72
Pt	1245	16.74
Ag	2160	4.35
Ti	609	11.46
V	1248	14.67
W	1551	14.61

permittivity of metals at the THz frequency band. For example, from (2.9) the permittivity of the gold can be found as $\epsilon_m = -1.22 \times 10^5 - j7.24 \times 10^5$ at the frequency of $f = 1$ THz which is much larger than its values at optical frequencies.

Now consider a surface plasmon polariton mode propagating on a metal-dielectric interface. From (2.6):

$$k_z = k\sqrt{\frac{\epsilon_m \epsilon_d}{\epsilon_m + \epsilon_d}} = k_z' - jk_z'' \tag{2.10}$$

it can be seen from this relation that when $\mid \epsilon_m \mid \gg \mid \epsilon_d \mid$, the z component of the propagation constant of surface plasmon polaritons, i.e. k_z will be close to the propagation constant in the dielectric medium k. For example if the metal and dielectric are chosen to be gold and air, then at the frequency of $f = 1$ THz, (2.10) gives:

$$k_z = k(1 + 1.05 \times 10^{-7} - j6.74 \times 10^{-7}) = k_z' - jk_z'' \tag{2.11}$$

thus

$$k_z' \approx k \tag{2.12}$$

$$k_z'' = 6.74 \times 10^{-7} k \tag{2.13}$$

and the x component of the propagation constant in the dielectric medium can be calculated as (see Fig. (2.1) for coordinate system orientation):

$$\gamma_d = \sqrt{k_z^2 - k^2} = (8.9 - j7.6) \times 10^{-4} k = 18.6 - j15.9 \tag{2.14}$$

and the propagation depth into dielectric which is the most important parameter in the applications such as sensing, imaging and enhanced nonlinear phenomena on the surface which rely on the field confinement, can be found as:

$$L_d = \frac{1}{2\mathrm{Re}(\gamma_d)} = 89.7\lambda = 2.7cm \tag{2.15}$$

by comparing this value with the value of L_d at optical frequencies which is smaller than a wavelength, it can be concluded that not only the fields are not confined to the surface, but also they are weakly guided and any imperfections in the surface can result in decoupling of the fields from the metal-dielectric interface.

Equation (2.13) shows that the imaginary part of the propagation constant is small and therefore the propagation length of the surface plasmon polaritons will be large in the THz band:

$$L = \frac{1}{2k_z''} = 1.18 \times 10^5 \lambda = 35.4m \tag{2.16}$$

This means that surface plasmon polaritons are very low loss waves in the terahertz band. This result was expected because as it was mentioned its fields are not confined on the surface and most of the energy is in the dielectric medium which assumed to have negligible loss. Because of this low loss property, guiding of the THz wave outside of a bare metallic cylinder has been proposed [22]. Although these kind of waveguides have very small material loss, the loss duo to surface imperfection, bends, non-uniformities, or nearby objects can be very severe and limits their applications.

2.2.2 Candidates for guiding THz surface plasmon polaritons

It was shown in the previous section that metals can not be used for guiding confined surface plasmons at THz frequencies as they are commonly used in the optical region of

the spectrum. In this section we will consider other candidates which can be used instead of them.

Lets review the results of the previous section, it was found that the large value for the permittivity of metals lead to the weak confinement of the surface plasmon polaritons to a metal-dielectric interface. Looking at (2.9) it is obvious that this is the case whenever $\omega \ll \omega_p$ and the data in the table (2.1) shows that the plasma frequency for metals lies in the visible and ultraviolet regions of EM spectrum. Therefore, conductors with smaller plasma frequencies are needed for guiding THz surface plasmon polariton waves.

Equation (2.2) shows that the plasma frequency is proportional to the square root of the carrier density n and it is well known, in semiconductors carrier density can be controlled by changing the doping level. This fact makes doped semiconductors a candidate for confined surface plasmon guiding at THz band. Some researchers have measured the permittivity of doped semiconductors at THz frequencies using time domain spectroscopy system [4, 9]. In [4] a 0.92 Ωcm P-type and a 1.15 Ωcm N-type doped silicon have been investigated. After fitting the measurement results with Drude model, the plasma and collision frequency of $f_p = 1.75$ THz and $f_t = 1.51$ THz for N-type and $f_p = 1.01$ THz and $f_t = 0.64$ THz for the P-type have been found. As these values for the collision and plasma frequencies indicate, the ratio of plasma frequency to collision frequency is in the order of unity for doped semiconductors. This will yield to a lossy dielectric with positive real part of the permittivity and cannot be used for guiding surface plasmon polaritons with strong confinement to the semiconductor-dielectric interface and large propagation length.

Another candidate for guiding confined surface waves which behave similar to surface plasmon polaritons in the THz band is periodically structured metal. It is well known in the microwave community that a metal surface which has periodic structure (for example a corrugated surface) can support surface waves [3]. Periodically structured metal surfaces create an impedance boundary condition and by properly designing the corrugation, a confined surface wave can be guided. The surface waves guided by these structures will be called *surface plasmon polariton-like surface waves* or surface waves for simplicity. Some authors have also called them *spoof surface plasmon polaritons*. Recently several researchers have considered these kinds of surfaces and showed that they can guide spoof surface plasmon in the terahertz region [12, 6]. In the next chapters these kinds of structures will be investigated for guiding surface plasmon polariton-like surface waves.

Chapter 3

Surface Waves Supported by Periodically Structured Metallic Surfaces

As it was discussed in the previous chapter, unlike optical surface plasmons, THz surface plasmons are not highly confined to the metal-dielectric interface due to large permittivity of metals at THz frequencies.

However, it is well known that a metallic corrugated surface is able to guide surface waves [5, 3]. Surface waves propagating on a patterned metallic surface have been used in designing antennas and slow wave structures. [5, 3] have discussed theoretical methods for analyzing these kinds of surface waves when the period of the periodic corrugation is much less than the free space wavelength of the field. More recently, [20] has used similar analysis method to show an effective surface impedance model for these surfaces and to propose application of these surfaces for guiding surface waves which have similar properties as surface plasmon polaritons.

In this chapter, a novel metallic two dimensional photonic crystal structure is proposed that can support strongly confined surface waves at THz frequencies. It is shown that the proposed structure supports surface waves which are highly confined to its surface. Band diagram and dispersion curves for the excited plasmonic modes are derived from full wave EM simulations. ATR technique is used to excite CW THz surface plasmonic waves on the proposed structure. It is shown that the structure can be used as a sensor for refractive index sensing and its sensitivity to a change in the refractive index of the sample is defined and it is demonstrated that the sensitivity is proportional to the group delay of surface

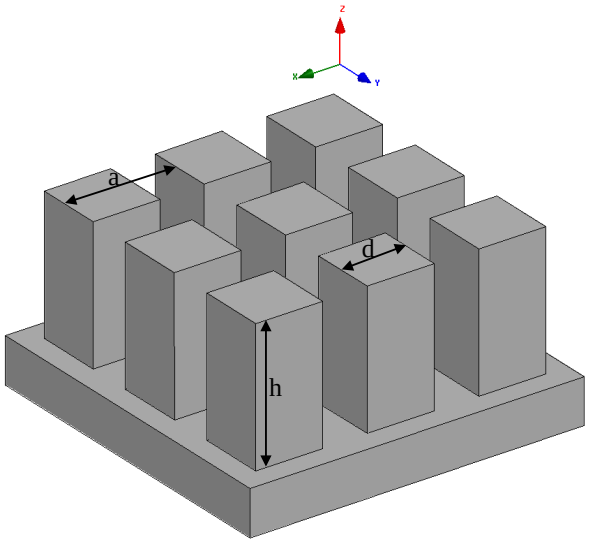

Figure 3.1: Proposed metallic periodic structure. The columns are $30\mu m \times 30\mu m \times 60\mu m$ ($d = 30\mu m$ and $h = 60\mu m$) and the period of the structure is $a = 50\mu m$.

mode.

3.1 Proposed Periodic Structure for Guiding Surface Waves

Fig. 3.1 shows the proposed structure which is composed of an array of square metallic columns made on a metallic substrate. The columns are $30\mu m \times 30\mu m \times 60\mu m$ ($d = 30\mu m$ and $h = 60\mu m$) and the period of the structure is $a = 50\mu m$. Assuming that the structure is made of a good conductor with large conductivity, The structure can support surface wave modes. These modes are confined to the surface of the structure and can propagate in any direction on the surface of this two dimensional metallic photonic crystals.

The fields of the first guided surface mode of the proposed structure is found by full wave simulation (the simulation method is explained in the next section) of a single cell. Fig. 3.2 shows magnitude and vector of the electric field on the $X - Z$ plane at frequency of $f = 1$THz for a surface mode propagating in the $\hat{x}$ direction. As it can be seen in this figure, the electric field is highly confined to the surface and is highly enhanced at the edges and corners of the metallic columns. Free space wavelength at the frequency of

$f = 1\text{THz}$ is $\lambda_0 = 300\mu m$ and the fields are localized to a region about $\frac{\lambda_0}{10}$ thick above the surface of the device. High confinement and large field enhancement at the surface are two main properties that made surface plasmon polaritons interesting at optical frequency. The surface mode of the proposed structure shows similar characteristics and its field distribution has common features with the field distribution of surface plasmon polariton modes at optical frequencies.

3.1.1 Simulation Method for Band Diagram Calculation

Simulations were performed using Ansoft HFSS$^{\text{TM}}$ which is a commercial 3-D Finite Element based electromagnetic simulator software. For finding band diagram of a surface wave mode, one cell of the structure has been simulated (Fig. 3.3). The columns and the substrate are assumed to be made of perfect electric conductor, which is a good approximation for most metals in the THz frequency band.

Periodic boundary condition is used on sidewalls and the structure is terminated with a perfectly matched layer (PML) in the vertical direction. The PML is placed $200\mu m$ above the columns to eliminate its effects on the field distribution. The phase difference between two sidewalls is assumed to be Φ_x for the walls with normal vector in the $\hat{x}$ direction and Φ_y for the walls with normal vector in the $\hat{y}$ direction (see the top view of the structure in Fig. 3.4).

With these boundary conditions, eigen-frequency solver of HFSS is used to find fields and frequency of the surface wave mode. Eigen-frequency solver is commonly used for determining resonant modes of a resonator. It solves an eigenvalue problem (resonator without the source) and finds fields and a complex valued frequency for the resonant mode. The imaginary part of the resonance frequency is nonzero for lossy (structure with radiation or material loss) structures and a quality factor Q defined as $Q = \frac{\text{Mag}(f)}{2\text{Imag}(f)}$ is also being calculated by the software.

By changing the values of Φ_x and Φ_y band diagram can be constructed point by point. Fig. 3.5 shows the band diagram of the two first surface wave mode of the structure shown in Fig. 3.1 that has been calculated by this method. As it can be seen there is a band gap between these two modes. The dispersion curve of the first surface mode that propagated in the $\hat{x}$ direction (the part of the diagram between Γ and χ), becomes almost flat near χ and as it will be discussed later, this response is desirable for sensing applications.

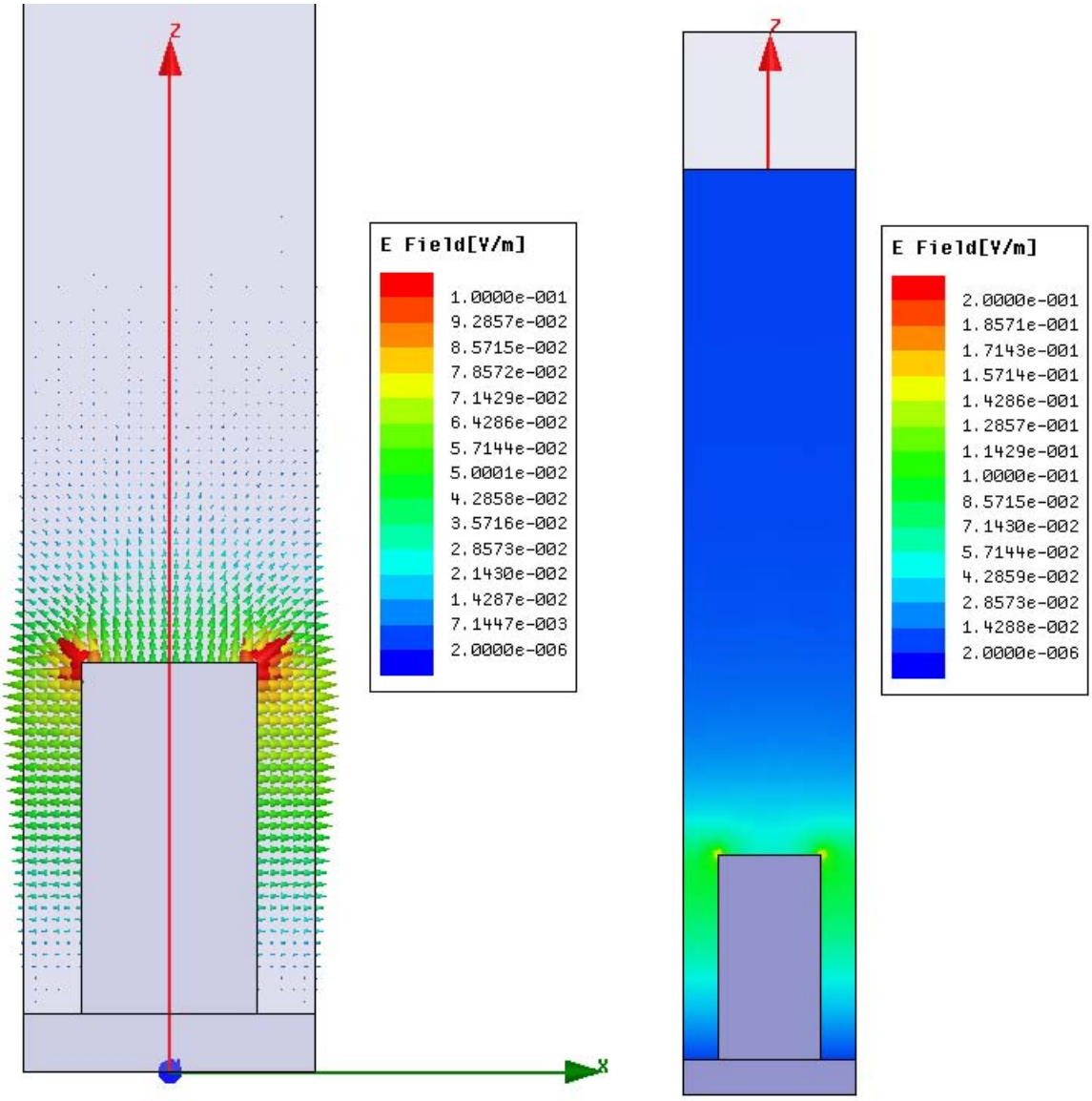

Figure 3.2: Magnitude (right) and vector(left) of the electric field on the $X - Z$ plane at frequency of $f = 1$THz for a surface mode propagating in the $\hat{x}$ direction.

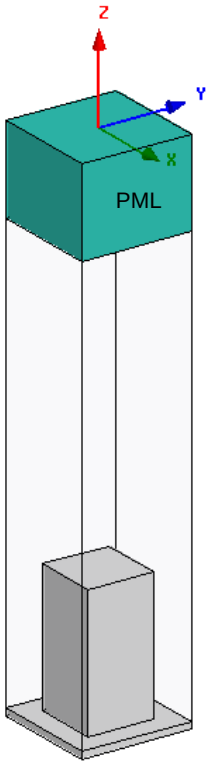

Figure 3.3: One cell of the periodic structure which was simulated for calculation of the band diagram of surface waves. Perfectly matched layer (PML) was used in the top of the cell to model infinite space above the cell.

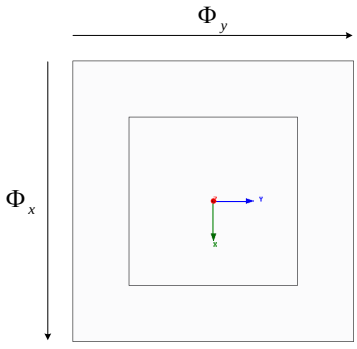

Figure 3.4: The phase difference between two sidewalls of a cell, Φ_x for the walls with normal vector in the $\hat{x}$ direction and Φ_y for the walls with normal vector in the $\hat{y}$ direction.

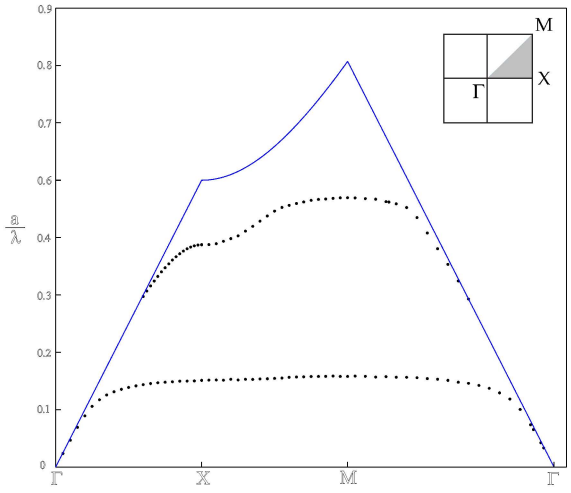

Figure 3.5: Band diagram of the two first surface wave mode of the structure shown in Fig. 3.1.

3.2 Prism Coupling to Surface Waves

Due to the fact that guided surface modes' propagation constants are larger than the free space wavenumber k_0, they should be excited by an inhomogeneous plane wave in an ATR configuration. Fig. 3.6 shows Otto's configuration for coupling of a TM polarized beam to the surface wave propagating in the $\hat{x}$ direction. For an incident CW THz beam, the power of the reflected beam is expected to show a minimum at the coupling angle θ_c for which the phase matching condition of $k_x = n_p k_0 \sin(\theta_c)$ is satisfied, in this relation n_p is the refractive index of the prism and k_x is the propagation constant of the guided surface mode. The prism coupling has been explained in details in the next chapter.

3.3 Application as a THz Sensor

The coupling angle in Fig. 3.6 is extremely sensitive to the refractive index of the medium between the prism and the metal surface. Therefore, a periodic structure with Otto's coupling configuration can be used as a sensor to measure the dielectric constant of the sample material placed between prism and the metallic surface. For having a quantitive

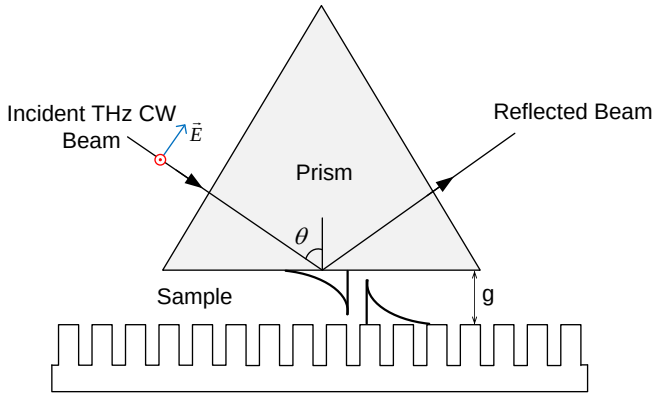

Figure 3.6: Otto's configuration for coupling of a TM polarized beam to the surface wave propagating in the $\hat{x}$ direction.

measure of sensitivity of a sensor made based on this configuration, a sensitivity parameter can be defined as:

$$S = \frac{\partial \theta_c}{\partial n_{sample}} \tag{3.1}$$

from the matching condition:

$$\sin\theta_c = \frac{k_x}{n_p k_0} \tag{3.2}$$

and taking partial derivative with respect to the sample refractive index from both side of (3.2) gives:

$$\cos\theta_c \frac{\partial \theta_c}{\partial n_{sample}} = \frac{1}{n_p k_0} \frac{\partial k_x}{\partial n_{sample}} \tag{3.3}$$

and thus:

$$S = \frac{\partial \theta_c}{\partial n_{sample}} = \frac{1}{n_p k_0 \cos(\theta_c)} \frac{\partial k_x}{\partial n_{sample}} \tag{3.4}$$

Assuming that the sample that is to be sensed fills the space between and above the columns (in practice it is sufficient to only fill the regions near the surface where the field is strong), the propagation constant of a the surface mode should be found by solving the following equation ($k_{sample} = n_{sample} k_0$):

$$\nabla^2 \mathbf{E} + k_{sample}^2 \mathbf{E} = 0 \tag{3.5}$$

it should be noticed that k_x will be only a function of the wavenumber in the sample medium and therefore multiplication of ω and n_p:

$$k_{sample} = n_{sample} k_0 = n_{sample} \frac{\omega}{c} \tag{3.6}$$

where c is the speed of light in vacuum.

Partial derivative of propagation constant with respect to the refractive index of the sample can be written as:

$$\frac{\partial k_x}{\partial n_{sample}} = \frac{dk_x}{dk_{sample}} \frac{\partial k_{sample}}{\partial n_{sample}} = \frac{dk_x}{dk_{sample}} \frac{\omega}{c} \tag{3.7}$$

and,

$$\frac{dk_x}{dk_{sample}} = \frac{\frac{\partial k_x}{\partial \omega}}{\frac{\partial k_{sample}}{\partial \omega}} = \frac{\partial k_x}{\partial \omega} \frac{c}{n_{sample}} \tag{3.8}$$

and thus (3.7) becomes:

$$\frac{\partial k_x}{\partial n_{sample}} = \frac{\omega}{n_{sample}} \frac{\partial k_x}{\partial \omega} = \frac{\omega}{n_{sample}} \tau \tag{3.9}$$

where τ is the group delay of the surface mode. Plugging in $\frac{\partial k_x}{\partial n_{sample}}$ from (3.8) into (3.9) leads to:

$$S = \frac{c}{n_{sample} n_p \cos(\theta_c)} \tau \tag{3.10}$$

From (3.10) it can be observed that sensitivity is proportional to the group delay of the excited surface mode. In other words, the sensitivity is proportional to the time interval over which the fields of the surface wave and the sample interact. Therefore, for maximum sensitivity, the operation frequency should be set in the flat part of the dispersion curve, where the group delay is maximum and the group velocity is close to zero. Fig. 3.7 shows the dispersion curve for the first surface wave mode on the proposed structure which has been calculated using eigenmode solver of the HFSS using the method described in section 3.1.1 (because $\Phi_y = 0$ for waves propagating in the $\hat{x}$ direction, from now on Φ_x has been represented by Φ for simplicity). Noticing that:

$$\frac{\partial k_x}{\partial \omega} = \frac{1}{2\pi a} \frac{d\Phi}{df} \tag{3.11}$$

(3.10) can be written as:

$$S = \frac{c}{n_{sample} n_p \cos(\theta_c)} \frac{1}{2\pi a} \frac{d\Phi}{df} \tag{3.12}$$

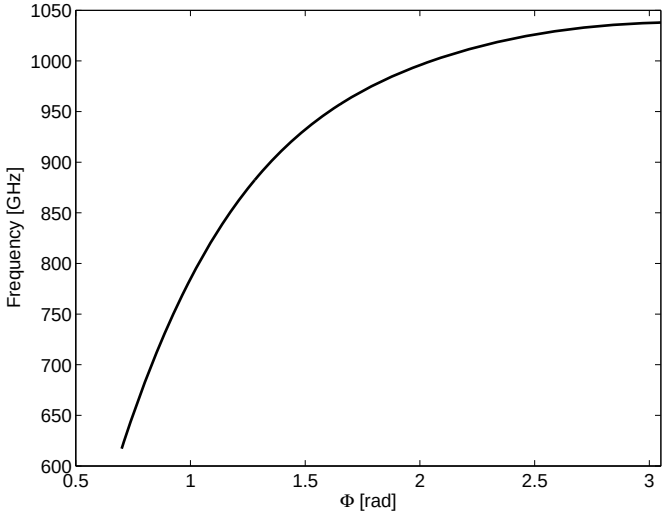

Figure 3.7: Dispersion curve for the first surface wave mode on the proposed structure.

Fig. 3.8 shows $\frac{d\Phi}{df}$ which is calculated by fitting a polynomial to the discrete points of dispersion relation and calculating the derivative of the fitted polynomial. As it can be seen from this diagram, $\frac{d\Phi}{df}$ is an increasing function of Φ. For $n_p = 3.42$ (silicon prism), and $a = 50\mu m$ at the frequency of $f = 1$THz, $\Phi = 2.05$ (from Fig. 3.7) gives $\theta_c = 34.9°$. From Fig. 3.8, $\frac{d\Phi}{df} = 1.26 \times 10^{-11}$ at $\Phi = 2.05$ and the sensitivity is calculated using (3.10) as $S = 245.8°$.

The sensitivity of the coupling angle with respect to the sample refractive index can also be calculated by simulation of plane wave incidence on the air-prism incidence and finding a minimum in the reflected field. Fig. 3.9 shows the amplitude of the reflected plane as function of the incident angle θ for different values of the sample permittivity. The gap width g between the prism and the metal surface should be adjusted carefully to achieve an efficient coupling. From simulation, the optimum value for g is found to be $g = 45\mu m$ for the structure made of silver with conductivity of $\sigma = 5.8 \times 10^7$. Because of the prism presence, the coupling angle has been changed from 34.9° to 37°. The sensitivity parameter can be found from this figure to be $S \approx 250°$ which is in good agreement with the value found from (3.10). With 0.1 degrees accuracy in the measurement of θ, it is possible to sense a change as small as 4×10^{-4} in the refractive index of the sample under test.

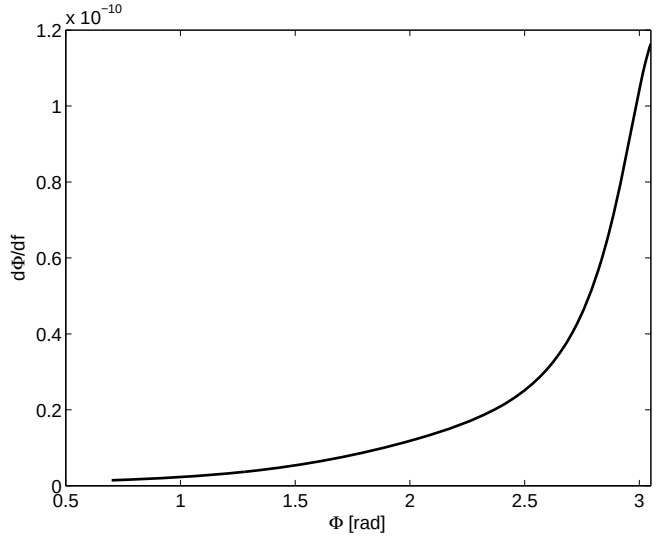

Figure 3.8: $\frac{d\Phi}{df}$ for the first surface mode of the structure of Fig. 3.1.

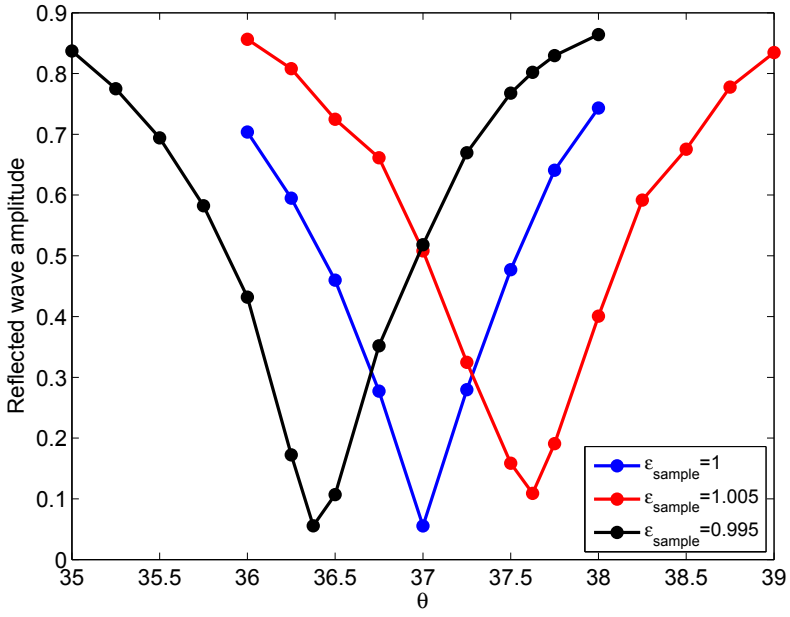

Figure 3.9: Amplitude of the reflected plane for different values of the sample permittivity.

Chapter 4

Analysis of Prism Coupling to Surface Plasmon-like Surface Waves

In this chapter a scattering parameter formulation is developed for modeling prism coupling to surface waves guided on a periodic structure (see Fig. 4.1). Although the model is general and can be applied and extended to a wide variety of problems, here the structure that was introduced in the previous chapter has been used for explaining and verification of the method.

4.1 Scattering Parameter Modeling of Prism Coupling to Periodic Structures

The method is based on the scattering parameters of one cell of the periodic structure and the prism above the structure. The prism is assumed to be large compared to the cell and is modeled as an infinite dielectric half space above the cell as shown in Fig. 4.2. Furthermore, it is assumed that the prism is far enough form the structure's surface so that the field distribution of the surface waves is not disturbed significantly. Furthermore, the structure is assumed to guide only one surface wave mode.

Considering these assumptions the fields entering and exiting a cell of the periodic structure on the left and right sides of each cell, can be approximated by linear combination of a plane wave incident on and reflected from the structure and the surface wave guided on the structure. The fields are normalized in a way that the squared absolute value of their amplitude represents the power carried by them. Fig. 4.2 shows these amplitudes

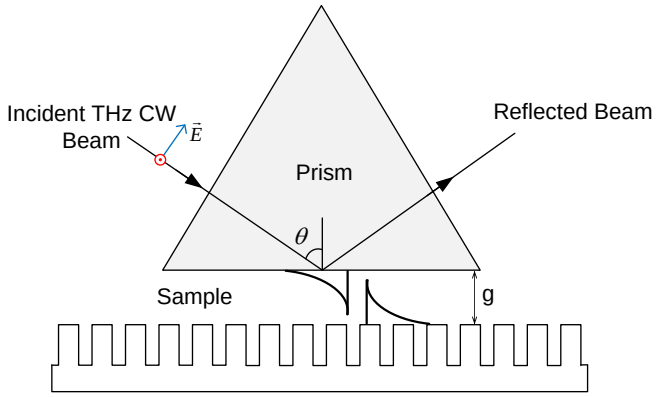

Figure 4.1: Prism coupling of a TM polarized beam to the surface wave propagating on a periodic structure.

and because of the linearity and reciprocal property of the structure, they can be related to each other as:

$$\begin{pmatrix} B_1 \\ B_2 \end{pmatrix} = \begin{pmatrix} t & \kappa \\ \kappa & r \end{pmatrix} \begin{pmatrix} A_1 \\ A_2 \end{pmatrix} \tag{4.1}$$

where κ is coupling coefficient, t is transmission coefficient of the surface wave, and r is reflection coefficient of the incident plane wave. For finding relations among these coefficients, a four port network model as shown in Fig. 4.3 can be used. Four port scattering parameter of matrix of the cell shown in Fig. 4.2 can be written as:

$$\begin{pmatrix} b_1 \\ b_2 \\ b_3 \\ b_4 \end{pmatrix} = \begin{pmatrix} 0 & r & \kappa & 0 \\ r & 0 & 0 & \kappa \\ \kappa & 0 & 0 & t \\ 0 & \kappa & t & 0 \end{pmatrix} \begin{pmatrix} a_1 \\ a_2 \\ a_3 \\ a_4 \end{pmatrix} \tag{4.2}$$

unitary property of scattering matrix of a lossless structure requires:

$$|r|^2 + |\kappa|^2 = 1 \tag{4.3}$$

$$r\kappa^* + \kappa t^* = 0 \tag{4.4}$$

$$2\angle\kappa - \angle r = \angle t + \pi \tag{4.5}$$

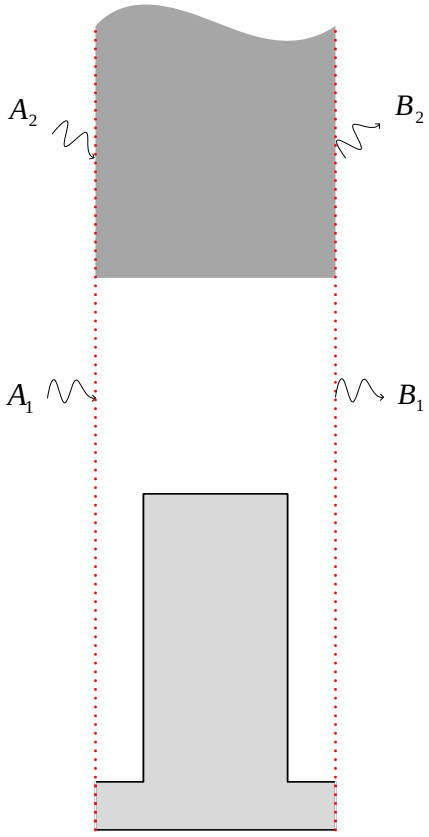

Figure 4.2: Schematic of the input and output waves of one cell of a periodic structure.

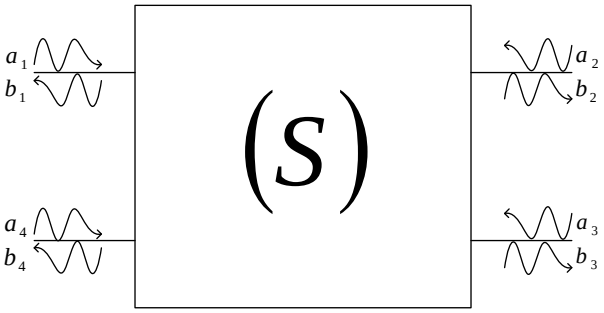

Figure 4.3: A four port network model for the cell shown in the Fig. 4.2.

For a lossless prism and a periodic structure with small loss and small coupling coefficient these equations remain approximately valid and the only correction to the transmission coefficient t due to loss is nonzero up to the fist order of approximation. Using the conservation of energy the equation for the absolute value the transmission coefficient is:

$$|t|^2 + |\kappa|^2 + P_{ln} = 1 \tag{4.6}$$

where P_{ln} is the power lost because of the material loss of the periodic structure when $|A_1| = 1$. There is also a correction to the phase of the transmission coefficient that will be explained in following sections.

4.2 Model Parameters Extraction

In this section a method is introduced for extraction of coupling parameters from results of EM simulations of a single cell. It will be shown that energy transport velocity and group velocity of a surface wave propagating on a periodic structure are the same. Using this result, formulas for calculation of coupling parameters will be derived.

4.2.1 Energy transport velocity

Electric and magnetic field of a surface wave propagating on a periodic structure at frequency ω_0 satisfy Maxwell's equations:

$$\nabla \times \mathbf{E_0} = -j\omega_0\mu\mathbf{H_0} \tag{4.7}$$
$$\nabla \times \mathbf{H_0} = j\omega_0\epsilon\mathbf{E_0} \tag{4.8}$$

and the fields at frequency ω the similar equations with ω_0 replaced by ω:

$$\nabla \times \mathbf{E} = -j\omega\mu\mathbf{H} \tag{4.9}$$
$$\nabla \times \mathbf{H} = j\omega\epsilon\mathbf{E} \tag{4.10}$$

(4.7) to (4.10) result in:

$$\nabla \cdot (\mathbf{H} \times \mathbf{E_0}^*) = j\omega\epsilon\mathbf{E} \cdot \mathbf{E_0}^* - j\omega_0\mu\mathbf{H_0}^* \cdot \mathbf{H} \tag{4.11}$$
$$\nabla \cdot (\mathbf{H_0}^* \times \mathbf{E}) = -j\omega_0\epsilon\mathbf{E_0}^* \cdot \mathbf{E} + j\omega\mu\mathbf{H} \cdot \mathbf{H_0}^* \tag{4.12}$$

adding (4.12) and (4.11) gives:

$$\nabla \cdot (\mathbf{H} \times \mathbf{E_0}^* + \mathbf{H_0}^* \times \mathbf{E}) = j(\omega - \omega_0)\epsilon \mathbf{E} \cdot \mathbf{E_0}^* + j(\omega - \omega_0)\mu \mathbf{H_0}^* \cdot \mathbf{H} \tag{4.13}$$

integrating both side of (4.11) over the volume of a cell (infinite in the direction perpendicular to the surface of the periodic structure):

$$\int_{\partial \mathcal{V}} (\mathbf{H} \times \mathbf{E_0}^* + \mathbf{H_0}^* \times \mathbf{E}) \cdot \mathbf{ds} = j(\omega - \omega_0) \int_{\mathcal{V}} \epsilon \mathbf{E_0}^* \cdot \mathbf{E} + \mu \mathbf{H} \cdot \mathbf{H_0}^* dv \tag{4.14}$$

where on the right hand side the Gauss theorem has been used to replace the volume integral with a surface integral over the cell boundaries. Assuming Floquet wavenumber of surface wave is given by $\mathbf{K} = K_x \hat{x} + K_y \hat{y}$ and noticing that the surface integral is zero on the structure's surface and the boundary at infinity (fields go to zero exponentially in the direction perpendicular to the structure surface), (4.14) can be written as:

$$\begin{aligned}
&(1 - \mathrm{e}^{-j(K_x - K_{x_0})a_x}) \int_{S_{X^-}} (\mathbf{H} \times \mathbf{E_0}^* + \mathbf{H_0}^* \times \mathbf{E}) \cdot \mathbf{ds} + \\
&(1 - \mathrm{e}^{-j(K_y - K_{y_0})a_y}) \int_{S_{Y^-}} (\mathbf{H} \times \mathbf{E_0}^* + \mathbf{H_0}^* \times \mathbf{E}) \cdot \mathbf{ds} = j(\omega - \omega_0) \int_{\mathcal{V}} \epsilon \mathbf{E_0}^* \cdot \mathbf{E} + \mu \mathbf{H} \cdot \mathbf{H_0}^* dv
\end{aligned} \tag{4.15}$$

where the surface integrals on four peripheral faces have been simplified to two integral on faces S_{X^-} and S_{Y^-} using Floquet theorem relation between fields on parallel faces. S_{X^-} and S_{Y^-} are surfaces of the cell with normal vectors in the $\hat{x}$ and $\hat{y}$ at lower value of x and y respectively. Now consider the limit when $\omega \to \omega_0$ and $K_x \to K_{x_0}$, so the following approximation can be made:

$$1 - \mathrm{e}^{-j(K_x - K_{x_0})a_x} \to j\Delta K_x a_x \tag{4.16}$$

$$1 - \mathrm{e}^{-j(K_y - K_{y_0})a_y} \to j\Delta K_y a_y \tag{4.17}$$

replacing these expressions in (4.15) with their approximate values, gives:

$$2P_x j\Delta K_x a_x + 2P_y j\Delta K_y a_y = j\Delta\omega(2W) \tag{4.18}$$

where P_x and P_y are average powers entering the cell from the S_{X^-} and S_{Y^-} surfaces respectively, and W is the stored power in the cell, that is:

$$P_x = \frac{1}{2}\mathrm{Re}\left\{\int_{S_{X^-}} \mathbf{E}\times\mathbf{H}^*\cdot\hat{x}ds\right\} \tag{4.19}$$

$$P_y = \frac{1}{2}\mathrm{Re}\left\{\int_{S_{Y^-}} \mathbf{E}\times\mathbf{H}^*\cdot\hat{y}ds\right\} \tag{4.20}$$

$$W = \frac{1}{2}\int_{\mathcal{V}} \epsilon|\mathbf{E}|^2 + \mu|\mathbf{H}|^2 dv \tag{4.21}$$

(4.18) can be further simplified as:

$$P_x a_x \frac{dK_x}{d\omega} + P_y a_y \frac{dK_y}{d\omega} = W \tag{4.22}$$

or,

$$\frac{P_x a_x}{v_{g_x}} + \frac{P_y a_y}{v_{g_y}} = W \tag{4.23}$$

where $v_{g_x} = \frac{d\omega}{dK_x}$ and $v_{g_y} = \frac{d\omega}{dK_y}$. For the case that the surface wave propagates only in the $\hat{x}$ direction, (4.23) reduces to:

$$v_{g_x} = \frac{a_x P_x}{W} \tag{4.24}$$

here v_{g_x} is the group velocity of the surface wave. The energy transport velocity is defined as:

$$v_{\mathcal{E}_x} \triangleq \frac{a_x}{T_x} \tag{4.25}$$

where T_x is the time that takes for the energy stored in a cell to be transported to its next cell, that is:

$$T_x = \frac{W}{P_x} \tag{4.26}$$

using this definition and (4.24) it is found that:

$$v_{\mathcal{E}_x} = \frac{a_x}{\frac{W}{P_x}} = \frac{a_x P_x}{W} = v_{g_x} \tag{4.27}$$

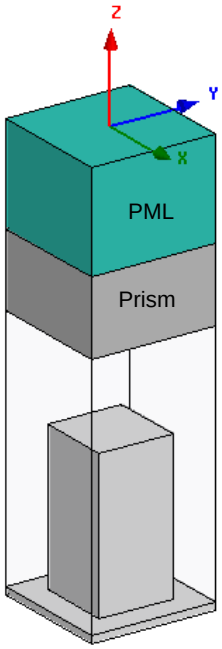

Figure 4.4: One cell of the periodic structure which contains a part of prism and one cell of the periodic surface.

therefore, for a surface wave propagating on a periodic structure, energy transport velocity and group velocity are equal.

4.2.2 Parameters calculation

Using the result of the previous section a method for extraction of coupling parameters from eigen-frequency simulation of a single cell can be devised that is explained in this section. Eigen-frequency simulation of one cell of the periodic structure and prism as shown in Fig. 4.4 is considered. Similar to what was assumed in the section 3.1.1, the periodic boundary condition is used on peripheral faces with Φ_x and zero phase shifts in the $\hat{x}$ and $\hat{y}$ directions. Furthermore, material loss due to the finite conductivity of metals is ignored. As a result of the radiation loss, a complex valued frequency and a quality factor Q_r can be found that sustain the fields in the cell.

The definition of the coupling coefficient κ is the ratio of the amplitude of radiated plane wave to the amplitude of the entering surface wave, that is:

$$|\kappa| = \left|\frac{B_2}{A_1}\right| \tag{4.28}$$

and absolute value of the radiated field mode is equal to the square root of radiated power:

$$|B_2| = \sqrt{P_{rn}} \tag{4.29}$$

and the stored energy in a cell can be found by use of (4.27):

$$W = |A_1|^2 T_x = |A_1|^2 \frac{a_x}{\frac{d\omega}{dK_x}} \tag{4.30}$$

and the quality factor Q_r,

$$Q_r = \omega \frac{W}{P_r} = \omega \frac{a_x |A_1|^2}{|B_2|^2 \frac{d\omega}{dK_x}} \tag{4.31}$$

thus, absolute value of coupling coefficient is given by:

$$|\kappa| = \sqrt{2\pi \frac{c}{v_g} \frac{a}{\lambda}} \frac{1}{\sqrt{Q_r}} = \sqrt{\frac{f}{\frac{df}{d\Phi}}} \frac{1}{\sqrt{Q_r}} \tag{4.32}$$

and $\frac{df}{d\Phi_x}$ can be calculated from the dispersion diagram of the mode.

Now consider simulation of a cell similar to the one shown in Fig. 4.4 but without the prism and with material loss of the metal. Using similar method of reasoning it can be shown that:

$$P_{ln} = \frac{f}{\frac{df}{d\Phi}} \frac{1}{Q_l} \tag{4.33}$$

where P_{nl}, as was defined in the section 4.1, is the amount of power lost due to material loss when $A_1 = 1$. By use of (4.3) and (4.6), the absolute value of other coupling parameters can be found as:

$$|r| = \sqrt{1 - \frac{f}{\frac{df}{d\Phi}} \frac{1}{Q_r}} \tag{4.34}$$

$$|t| = \sqrt{1 - \frac{f}{\frac{df}{d\Phi}} \frac{1}{Q_t}} \tag{4.35}$$

where Q_t is total quality factor defined as:

$$\frac{1}{Q_t} \triangleq \frac{1}{Q_r} + \frac{1}{Q_l} \tag{4.36}$$

ignoring the effect of coupling in the phase of reflected plane wave, the phase of the reflection coefficient can be approximated by the phase shift of a TM plane wave when it undergoes total internal reflection [21]:

$$\angle r = \frac{-1}{\sin^2(\theta_c)} \sqrt{\frac{\cos^2(\theta_c)}{\cos^2(\theta)} - 1} \tag{4.37}$$

and the phase of the transmission coefficient is equal to $-\Phi$ (the phase difference between two boundary faces with $\hat{x}$ normal). This phase shift is for a structure without material loss, small material loss leads to a small correction Φ_c which can be found from the simulation of the lossy structure without the prism (the one which was done for finding Q_l). Thus,

$$\angle t = -(\Phi + \Phi_c) \tag{4.38}$$

and the phase of the coupling coefficient can be calculated from (4.5):

$$\angle \kappa = \frac{\angle r + \angle t}{2} + \frac{\pi}{2} \tag{4.39}$$

The method described above is used for extraction of coupling parameters of the periodic structure proposed in the previous chapter at $f = 1$ THz for different values of g (the gap size between the prism and the structure's surface). It can be noticed that all the coupling parameters can be found by knowing the values of $\frac{df}{d\Phi}$, Φ_c, Q_l, κ, and Φ. The first three of these do not depend on the gap size. $\frac{df}{d\Phi}$ was found from the dispersion relation (Fig. 3.8) to be equal to 8.2×10^{10}, Φ_c, and Q_l were found from simulation of a cell without the prism but with metallic loss and were found to be equal to 0.03 rad and 231.4. Φ and κ are function of the gap size and have been calculated for few values of g by simulating a cell with prism on the top but without material loss. Figs. 4.5 and 4.6 show dependance of these to parameters on the gap size. Polynomial curves were fitted to the data and the fitted data are used in the following sections.

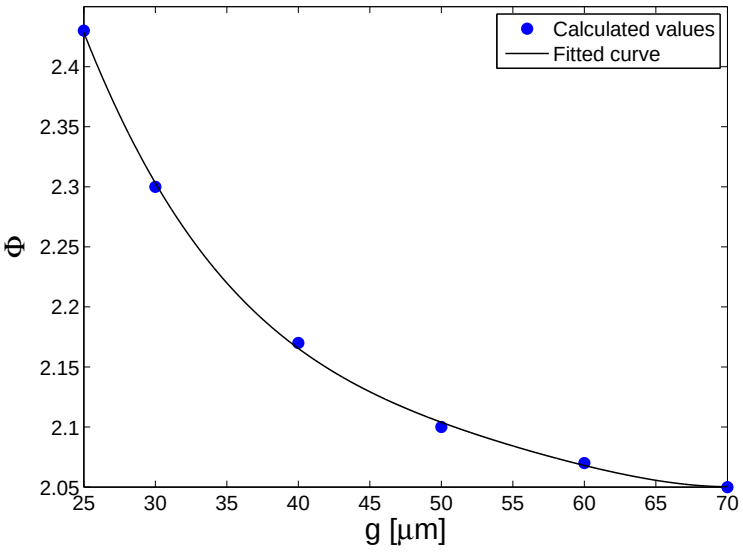

Figure 4.5: The phase difference between two parallel faces of the cell shown in the Fig. 4.4 as a function of gap size g at the frequency of $f = 1$ THz.

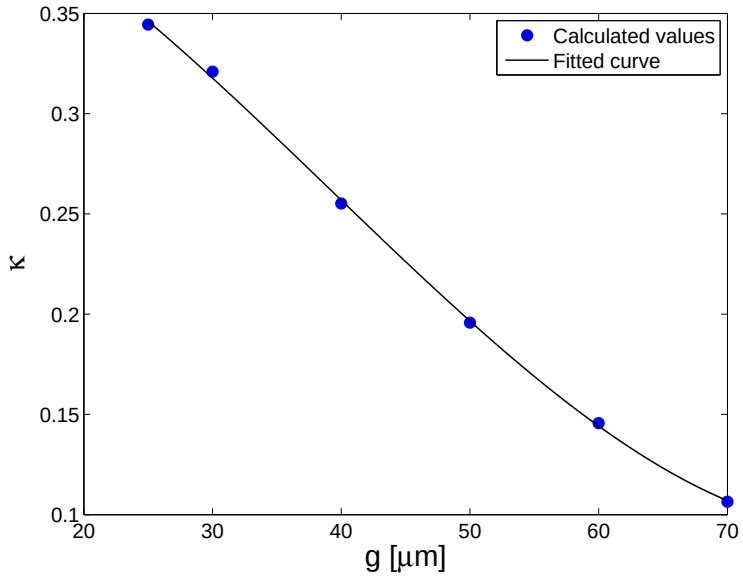

Figure 4.6: Coupling coefficient as a function of gap size g at the frequency of $f = 1$ THz.

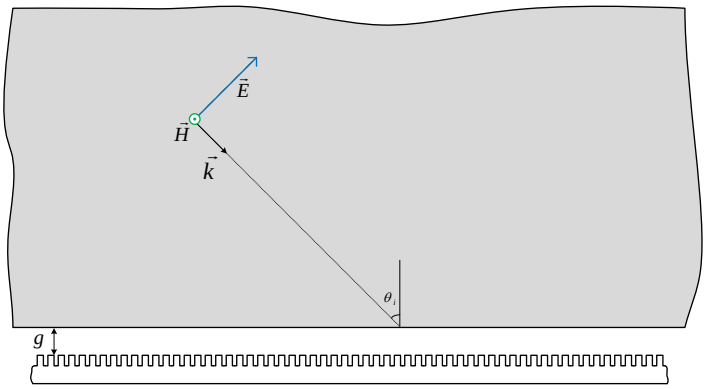

Figure 4.7: Coupling of a TM polarized plane wave to a source wave mode of a periodic structure.

4.3 Coupling of Plane Waves to a Periodic Structure

Using the scattering parameter formulation introduced in previous sections for a single cell, coupling of a plane wave to the surface waves can be modeled. The results has been compared to EM simulation results of the structure performed in Ansoft HFSS and good agreement between them verifies the validity of the scattering parameter model.

Consider a plane wave is shone on an infinite periodic structure as shown in Figs. 4.7. For each cell of the periodic structure input and output waves are related by (4.1):

$$\begin{pmatrix} B_1 \\ B_2 \end{pmatrix} = \begin{pmatrix} t & \kappa \\ \kappa & r \end{pmatrix} \begin{pmatrix} A_1 \\ A_2 \end{pmatrix} \tag{4.40}$$

and due to infinite nature of plane wave a phase difference ϕ is dictated between two adjacent cells, therefore:

$$B_1 = e^{-j\phi} A_1 \tag{4.41}$$

$$\phi = k_0 n_p \sin(\theta_i) a \tag{4.42}$$

(4.1) and (4.41) lead to:

$$\begin{aligned} B_1 &= t e^{j\phi} B_1 + \kappa A_2 \\ B_2 &= \kappa e^{j\phi} B_1 + r A_2 \end{aligned} \tag{4.43}$$

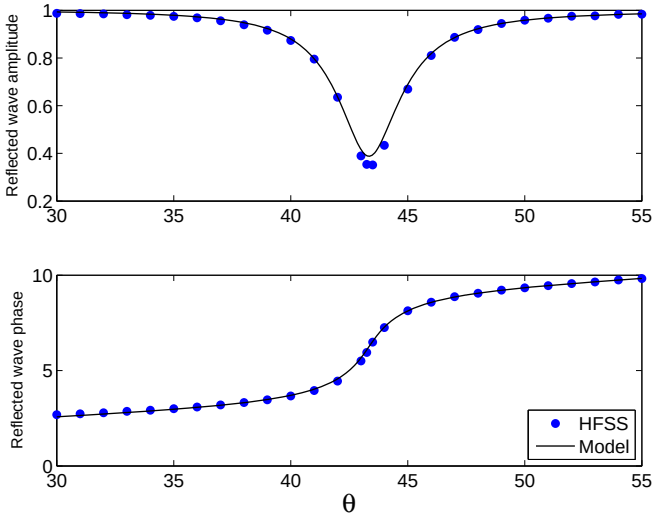

Figure 4.8: Magnitude and phase of the reflected plane wave for gap size of $g = 25\mu m$. Solid curve is the result obtained from the scattering parameter model and dots represent HFSS simulation results.

thus,

$$B_1 = \frac{\kappa}{1 - e^{j\phi}t} A_2 \tag{4.44}$$

$$B_2 = (r + \frac{\kappa^2 e^{j\phi}}{1 - e^{j\phi}t}) A_2 \tag{4.45}$$

(4.1) and (4.41) are reminiscent of well known equations of coupling of waves to a ring resonator and therefore, there is an optimum value for the gap size κ that critical coupling happens.

The model has been verified by comparing its results for plane wave incidence on the periodic structure of previous chapter to direct EM simulations in Ansoft HFSS. For HFSS simulations, Floquet port along with periodic boundary condition have been used. Figs. 4.8 to 4.14 show the results for the reflected wave B_2 calculated from the scattering parameter model and HFSS simulations.

Fig. 4.15 shows the amplitude of the reflected wave as a function of the incident angle for different values of gap size g. As it can be seen from this figure, the optimum value for the gap size is $45\mu m$.

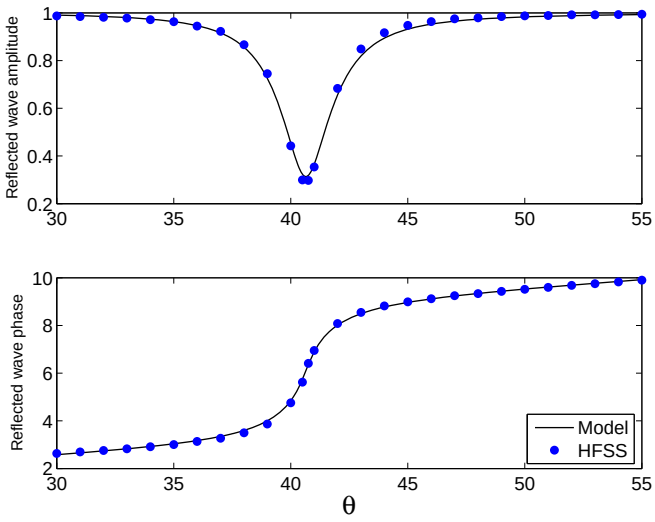

Figure 4.9: Magnitude and phase of the reflected plane wave for gap size of $g = 30\mu m$. Solid curve is the result obtained from the scattering parameter model and dots represent HFSS simulation results.

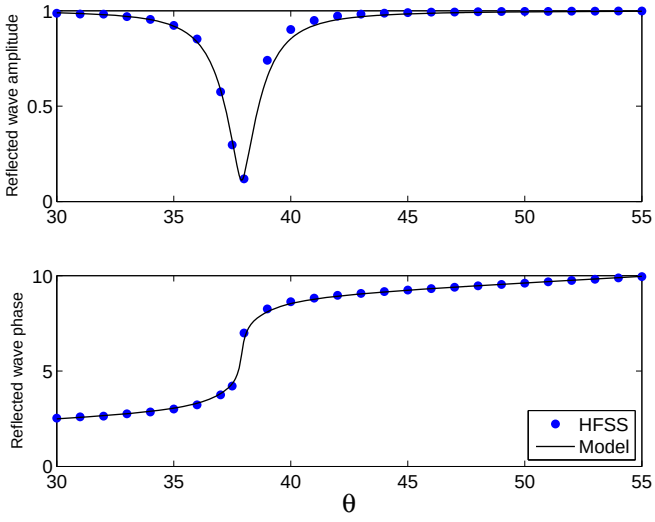

Figure 4.10: Magnitude and phase of the reflected plane wave for gap size of $g = 40\mu m$. Solid curve is the result obtained from the scattering parameter model and dots represent HFSS simulation results.

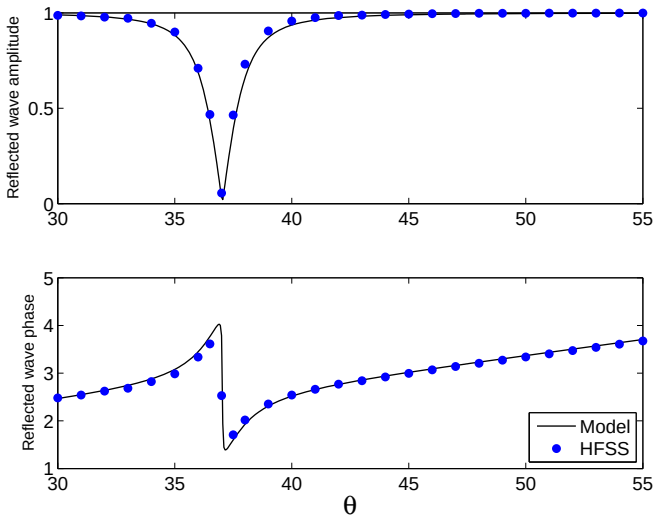

Figure 4.11: Magnitude and phase of the reflected plane wave for gap size of $g = 45\mu m$. Solid curve is the result obtained from the scattering parameter model and dots represent HFSS simulation results.

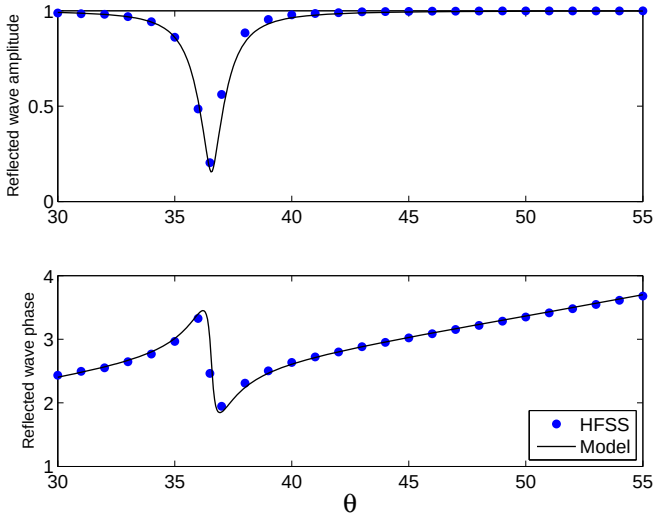

Figure 4.12: Magnitude and phase of the reflected plane wave for gap size of $g = 50\mu m$. Solid curve is the result obtained from the scattering parameter model and dots represent HFSS simulation results.

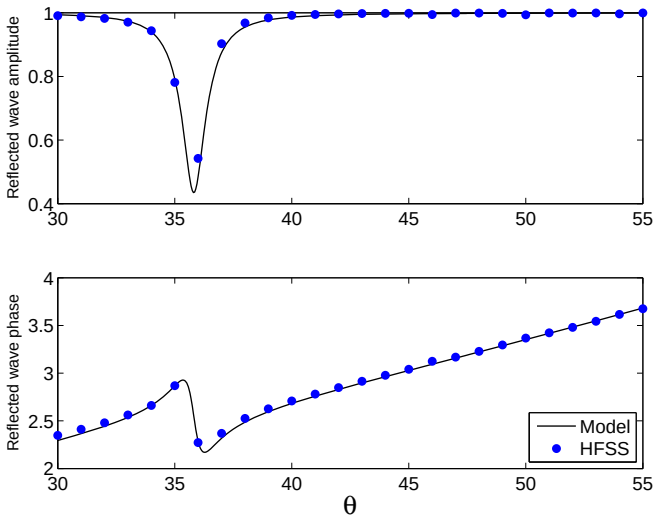

Figure 4.13: Magnitude and phase of the reflected plane wave for gap size of $g = 60\mu m$. Solid curve is the result obtained from the scattering parameter model and dots represent HFSS simulation results.

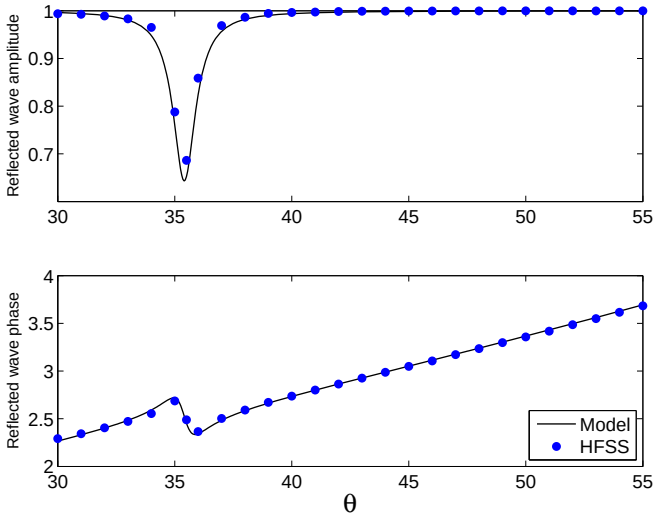

Figure 4.14: Magnitude and phase of the reflected plane wave for gap size of $g = 70\mu m$. Solid curve is the result obtained from the scattering parameter model and dots represent HFSS simulation results.

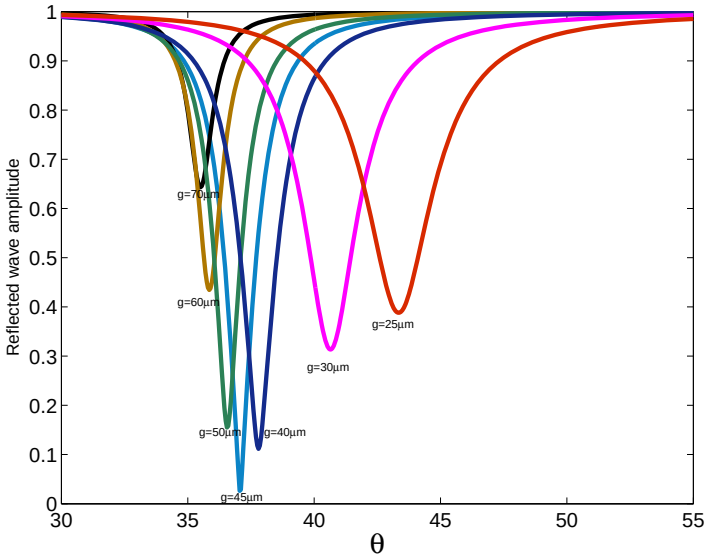

Figure 4.15: Magnitude of the reflected plane wave for different values of gap size obtained from the scattering parameter model.

4.4 Analysis of Gaussian Beam Coupling using PWE Method

In the previous section coupling of plane waves to the periodic structure using prism coupling was investigated. A plane wave has infinite extent and in most of applications the field incident on the structure can be better approximated by a Gaussian beam. In this section, coupling of a Gaussian beam to the surface wave mode of the structure using the Plane Wave Expansion (PWE) method is presented.

A scalar three dimensional Gaussian beam propagating along the z axis is given by[21]:

$$U(x,y,z) = \frac{W_0}{W(z)} e^{-\frac{x^2+y^2}{W(z)}} e^{-jkz - jk\frac{x^2+y^2}{2R(z)} + j\xi(z)} \tag{4.46}$$

where z_0 is the Rayleigh range, W_0 is the beam waist radius, $R(z)$ is the radius of curvature of wavefront, and $\xi(z)$ represents the phase retardation relative to a plane wave propagating in the z direction. These parameters are given by the following relations:

$$z_0 = \frac{\pi W_0^2}{\lambda} \tag{4.47}$$

$$W(z) = W_0\sqrt{1 + (\frac{z}{z_0})^2} \tag{4.48}$$

$$R(z) = z(1 + (\frac{z_0}{z})^2) \tag{4.49}$$

$$\xi(z) = \tan^{-1}(\frac{z}{z_0}) \tag{4.50}$$

and electrical field of a vectorial Gaussian beam is given by [21]:

$$\mathbf{E} = (\hat{x} - \frac{x}{z + jz_0}\hat{z})U(x, y, z) \tag{4.51}$$

A Gaussian beam can be expressed as superposition of plane waves propagating in different directions. Using (4.45) and (4.44) reflected and coupled field of each plane wave can be calculated and the result for different plane waves added together to constitute the total reflected and coupled fields.

4.4.1 Two Dimensional Gaussian Beam Incidence

A two dimensional Gaussian beam (a Gaussian beam without y dependance) is considered first (Fig. 4.16). The case of three dimensional beam is discussed afterward. Using spectral domain formulation a field can be expanded in terms of plane waves. Electrical field and its spectral domain representations are Fourier transform pairs:

$$\tilde{\mathbf{E}} = \frac{1}{2\pi}\int_{-\infty}^{\infty} \mathbf{E}e^{jk_x x}dx \tag{4.52}$$

$$\mathbf{E} = \int_{-\infty}^{\infty} \tilde{\mathbf{E}}e^{-jk_x x}dk_x \tag{4.53}$$

Spectral domain counterpart of the incident electrical field ($\tilde{\mathbf{E}}_\mathbf{i}$) on the $z = 0$ plane can be calculated using (4.52) and (4.46):

$$\tilde{\mathbf{E}}_\mathbf{i}dk_x = \frac{W_0 k}{2\sqrt{\pi}}e^{-(\frac{W_0 k\sin(\theta_d)}{2})^2}(\cos(\theta_i + \theta_d)\hat{X} + \sin(\theta_i + \theta_d)\hat{Z})d\theta_d \tag{4.54}$$

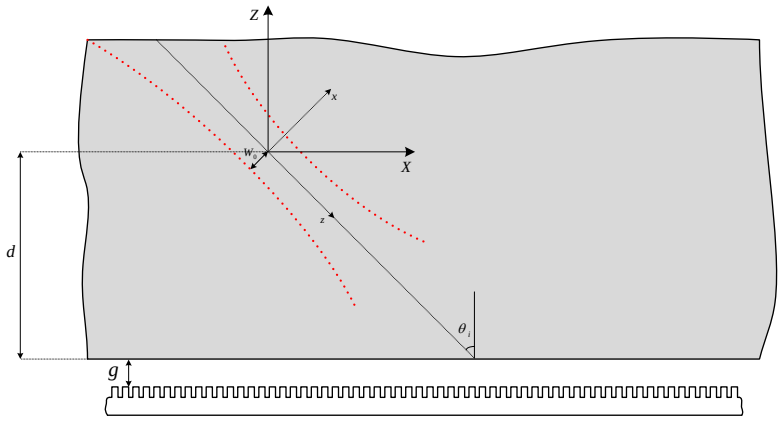

Figure 4.16: Coupling of a TM polarized Gaussian beam to a source wave mode of a periodic structure.

where θ_d is the angle between the direction of the propagation of the plane wave and axis of propagation of the beam, that is:

$$\sin(\theta_d) = \frac{k_x}{k} \tag{4.55}$$

The total electrical field can be calculated by adding the incident and reflected fields and are given by:

$$\mathbf{E} = \int (1 - Re^{-jk\cos(\theta_i+\theta_d)(2d)})\tilde{E_{i_x}}\hat{x} + (1 + Re^{-jk\cos(\theta_i+\theta_d)(2d)})\tilde{E_{i_z}}e^{-j(k_X X + k_Z Z)}\hat{z}d\theta_d \tag{4.56}$$

where the R is the reflection coefficient:

$$R = \frac{B_2}{A_2} = r + \frac{\kappa^2 e^{j\phi}}{1 - e^{j\phi}t} \tag{4.57}$$

$$\phi = k_0 n_p \sin(\theta_i + \theta_d)a \tag{4.58}$$

and $k_X = k\sin(\theta_i + \theta_d)$ and $k_Z = -k\cos(\theta_i + \theta_d)$ are $\hat{X}$ and $\hat{Z}$ components of wavevector of a constitutive plane wave of the field.

Equation (4.56) gives a closed form formula for the field of a Gaussian beam that illuminates the prism air interface. Only a one dimensional integral should be evaluated

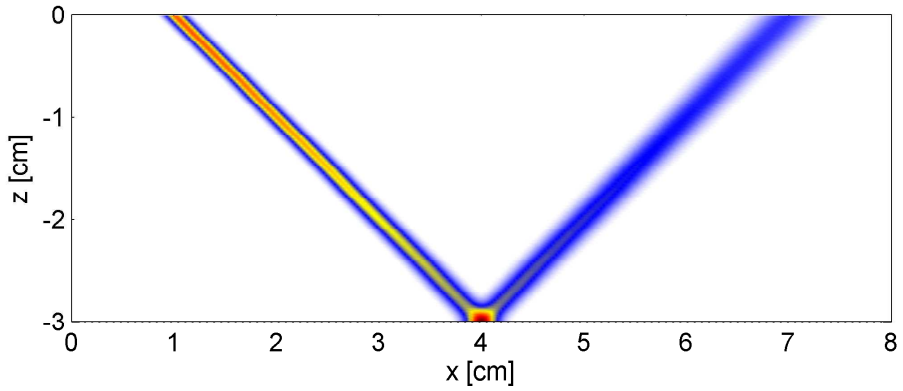

Figure 4.17: Absolute value of the electrical field squared found using PWE method with $\theta_i = 45°$ and $W_0 = 1000\mu m$.

numerically at different points of $X-Z$ plane. The integral has been calculated numerically in MATLAB for different values of incident angles and beam waist radii by using the values for coupling parameters that were calculated in previous sections. In all the results presented here the frequency is assumed to be $f = 1$THz and the gap size has its optimum value found previously i.e. $g = 45\mu m$. Fig. 4.17 shows the absolute value of the electrical field squared for $\theta_i = 45°$ and $W_0 = 1000\mu m$. As it can be seen in this figure, the field is almost completely reflected from the interface.

As it can be seen from Fig. 4.15 minimum reflection of a plane wave from the interface and minimum coupling to the surface wave happens when $\theta = 37.1°$. Fig. 4.18 shows the field of a Gaussian beam with $W_0 = 1000\mu m$ shone at $\theta = 37.1°$ on the structure. The figure shows that some part of the beam is coupled and the parts that are reflected are composed of two beam propagating in two directions making a small angle with each other. The reason for this phenomenon is the wide spectrum of incident wave in the spectral domain. The central part of the spectrum (plane waves propagating near θ_i) has been coupled to surface wave and two other remaining sides of the spectrum have been reflected back. If the incident Gaussian beam is more collimated, this means a beam with larger beam width radius, then almost all of the field can be coupled to the surface waves. Fig. 4.19 shows a beam with $W_0 = 6000\mu m$ and as it was expected the reflected field is negligible.

The coupled field can also be found by use of (4.44) and a similar procedure that was explained for the reflected field. Fig. 4.20 shows the absolute value of the coupled field (B_1) along with the incident field. The incident field is plotted four times larger to make the shift between two curves more clear.

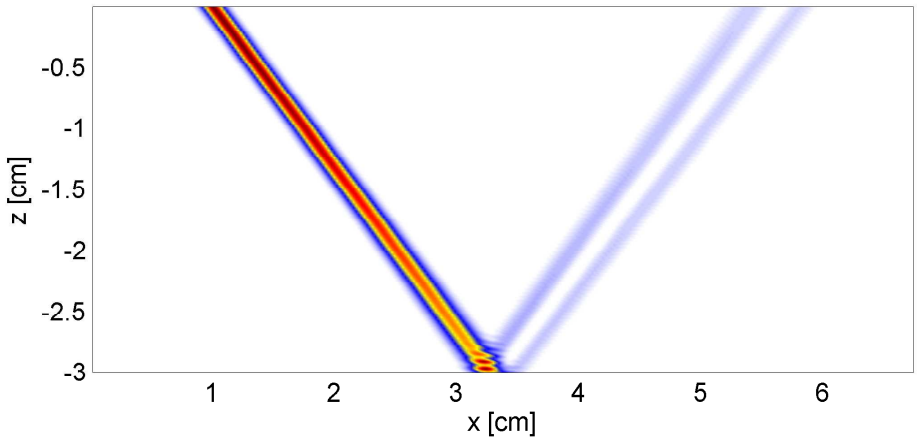

Figure 4.18: Absolute value of the electrical field squared found using PWE method with $\theta_i = 37.1°$ and $W_0 = 1000\mu m$.

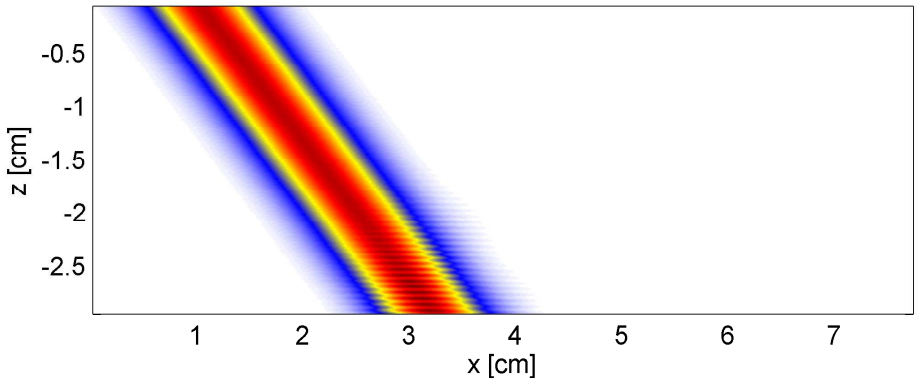

Figure 4.19: Absolute value of the electrical field squared found using PWE method with $\theta_i = 37.1°$ and $W_0 = 6000\mu m$.

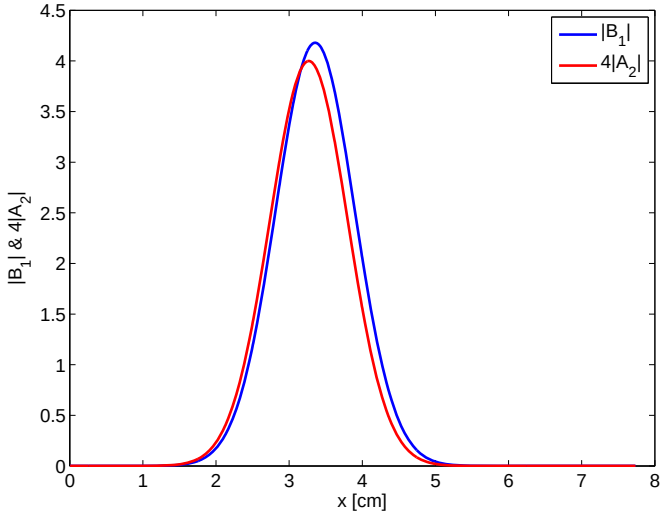

Figure 4.20: Absolute value of the coupled field (B_1) and the incident field. Note that The incident field is plotted four times larger.

4.4.2 Three Dimensional Gaussian Beam Incidence

The analysis of the interaction of a three dimensional beam with a periodic structure can also be performed with the PWE method. A three dimensional Gaussian beam can also be expanded in terms of plane waves that propagate in different directions. For a well collimated beam , spectral domain contents of the beam is only significant along the beam axis. In special case of the proposed structure the axis of the beam incident on the structure is in the $X-Z$ plane and therefore its spectral domain representation has significant value only for plane waves with small y direction wavevector components i.e. $k_y \ll k$, and only the value of the reflection coefficient R in vicinity of $k_y = 0$ is required for finding the reflected field. Due to symmetry of the structure with respect to the $X-Z$ plane, $R(k_y)$ and $R(-k_y)$ are equal and thus:

$$\frac{\partial R}{\partial k_y} = 0 \tag{4.59}$$

therefore spectral domain shape of a collimated beam will not change after reflection from the surface (it will just be multiplied by $R(k_y = 0)$. In other words, the variation of a three dimensional beam in the y direction will be preserved after reflection and its x direction variation will be same as that of a two dimensional beam discussed before.

4.5 Analysis of Gaussian Beam Coupling using LPWA Method

The interaction of a beam with a periodic structure can also be modeled by using Local Plane Wave Approximation (LPWA) which is explained in this section. This method is based on approximation of the incident field over one cell of the structure by a plane wave with amplitude equal to the incident field amplitude at the cell position and its angle determined by the phase difference of the cell with its neighbor. Therefore the key requirement for applying this method is the slow variation of the envelope of the incident field over the air prism interface.

If this requirement is met, the scattering parameter formulation introduced in section 4.1 can be used to describe the coupled and reflected field. More specifically the relation between incident, surface wave and reflected wave amplitudes for the n^{th} cell will be as:

$$B_{1_n} = tB_{1_{n-1}} + \kappa A_{2_n} \tag{4.60}$$

$$B_{2_n} = \kappa B_{1_{n-1}} + rA_{2_n} \tag{4.61}$$

for deriving (4.60) and (4.61) A_{1_n} has been replaced by $B_{1_{n-1}}$ because the surface wave entering the n^{th} cell is the wave that has left the $n-1^{th}$ cell. A_{2_n} is the amplitude of the incident wave at the cell position on the air-prism interface (e.g. at the middle of the cell) and the coupling parameters are determined by the gap size and the incident wave angle. These two recursive equations can be solved by assuming $B_{1_0} = 0$ (zero coupled surface wave) for a cell far enough from the beam incidence region.

Incident and reflected fields propagation in the prism can be performed using spectral domain formulation. Fast Fourier Transform has been used for calculation of the Fourier transform components of the field and for calculation of the inverse flourier transform. Fig. 4.21 shows the amplitude of the Z component (see Fig. 4.16 for the coordinate system orientation) of the reflected electrical field calculated by PWE and LPWA methods. The incident field is a two dimensional Gaussian beam with $W_0 = 6000\mu m$, the angle of incidence is $\theta_i = 37.1^\circ$, and the gap size $g = 45\mu m$. Fig. 4.21 shows the phase of the X component of the electrical field multiplied by $e^{k\sin(\theta_i)X}$ (to compensate for the fast varying part of the phase) along the air-prism interface. As it is clear from these plots, results of both methods are in good agreement with each other and this agreement verifies the validity of LPWA method.

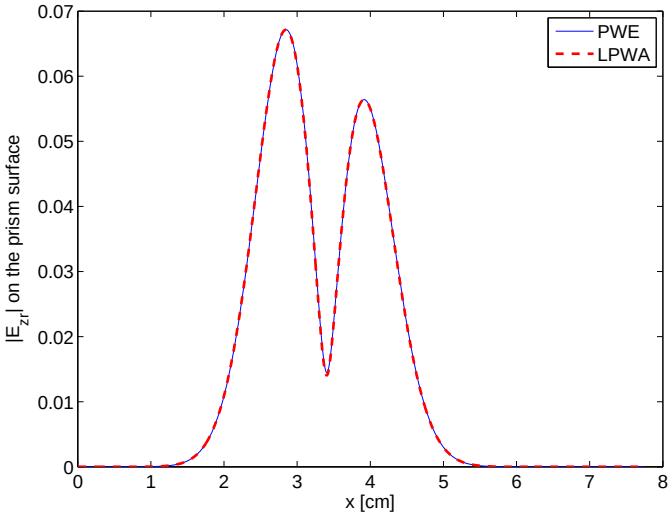

Figure 4.21: Magnitude of the Z component of the reflected electrical field calculated by PWE and LPWA methods.

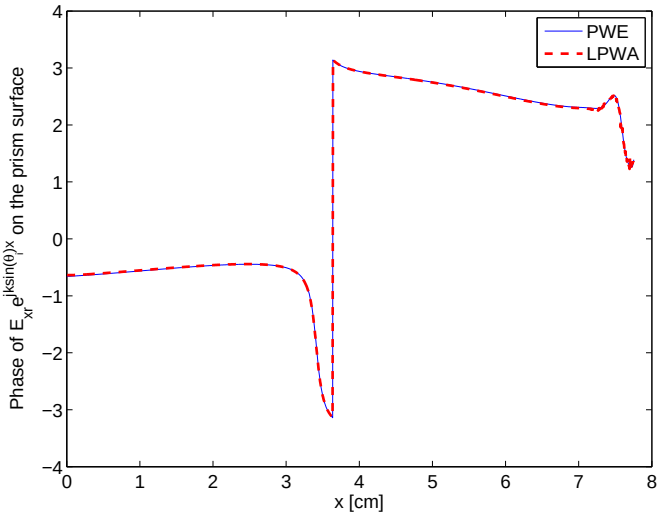

Figure 4.22: Phase of the X component of the reflected electrical field calculated by PWE and LPWA methods.

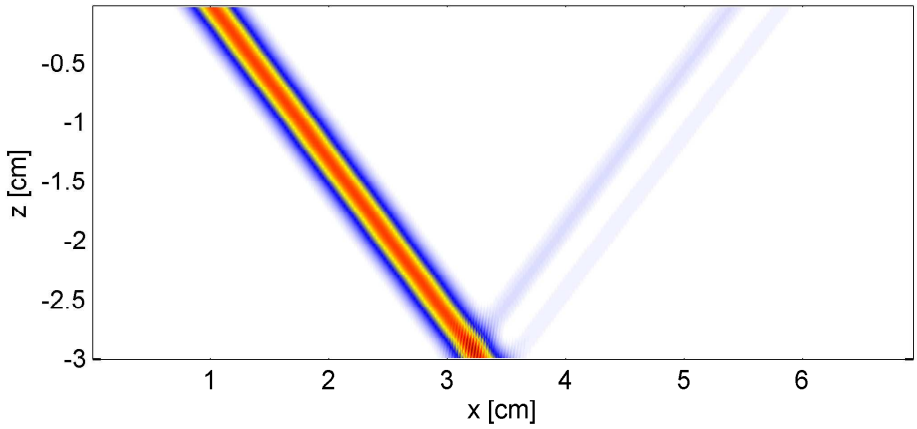

Figure 4.23: Absolute value of the electrical field squared found using LPWA method with $\theta_i = 37.1^\circ$ and $W_0 = 2000\mu m$.

Total electric energy of a Gaussian beam with $W_0 = 2000\mu m$ shone at $\theta_i = 37.1^\circ$ on the same periodic structure described above is calculated using LPWA method and is depicted on Fig. 4.23. Fig. 4.24 shows the same quantity that has been calculated by PWE method. The results from the two methods match pretty well which is another verification for the LPWA method. The main advantage of the LPWA method compared to PWE method is its capability for simulating aperiodic structures. For example consider a case where the prism is not parallel with the surface of the periodic structure and is tilted by a small angle θ_t (as shown in Fig. 4.25). In this case the whole device (prism and the periodic structure) is no longer periodic and the PWE method cannot be used for its simulation. However, LPWA method does not use the periodicity of the structure and can be used in this case. As long as the change in the gap size between the prism and the surface of the periodic structure remains small compared to its average value, coupling parameters for untilted prism can be used. These parameter can be calculated for different values of the gap size using the polynomial functions fitted to κ and Φ (Figs. 4.6 and 4.5). The absolute value of the X component of the reflected electrical field on the prism surface has been calculated and is plotted in Fig. 4.26 for the tilt angle of $\theta_t = 0.07^\circ$ and for the untilted prism ($\theta_t = 0.07^\circ$). The incident beam is assumed to be a Gaussian beam with $W_0 = 6000\mu m$ incident at the angle of $\theta_i = 37.1^\circ$ on the air-prism interface.

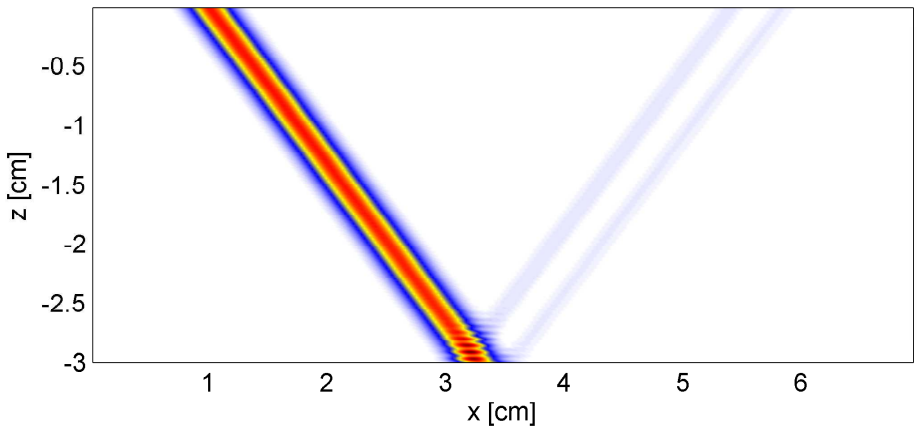

Figure 4.24: Absolute value of the electrical field squared found using PWE method with $\theta_i = 37.1°$ and $W_0 = 2000\mu m$.

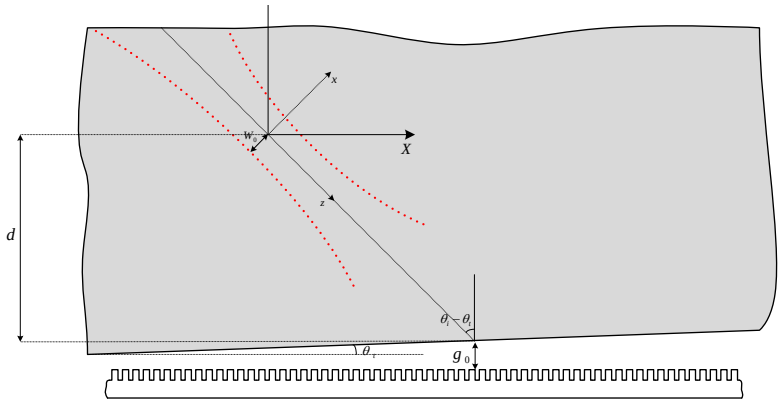

Figure 4.25: Coupling of a TM polarized Gaussian beam to a source wave mode of a periodic structure using a tilted prism.

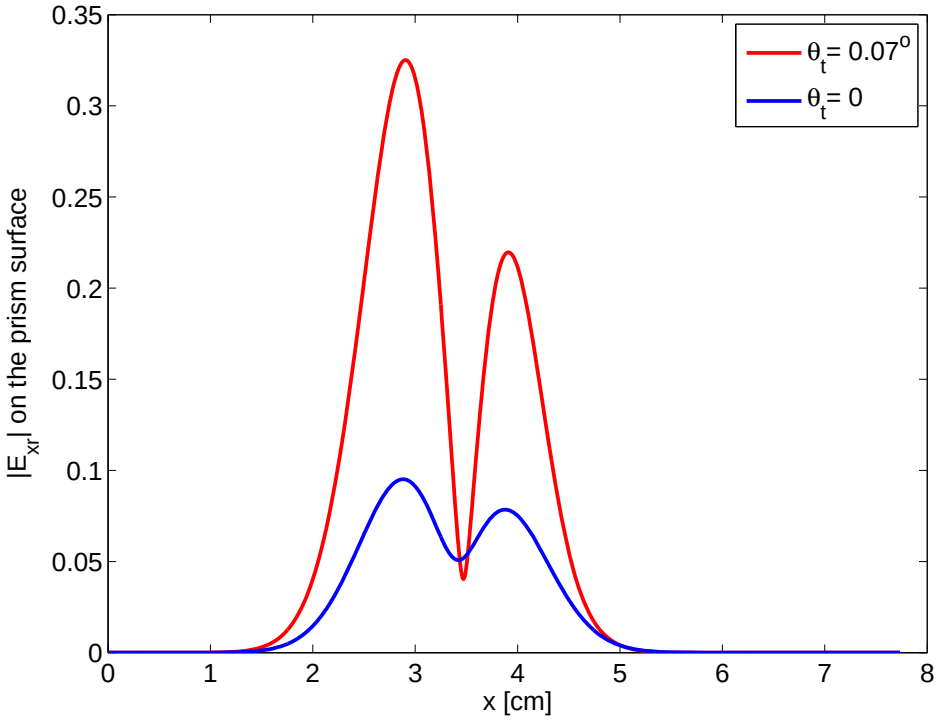

Figure 4.26: Magnitude of the X component of the reflected electrical field on the prism surface for the tilt angle of $\theta_t = 0.07^\circ$ and the untilted prism.

Chapter 5

Device Fabrication and Experimental Setup

5.1 Device Fabrication and Characterization

In this chapter details of fabrication and experimental setup designed for coupling surface waves on the structure proposed in previous chapters is presented.

The proposed structure, Fig. 5.1, as was discussed earlier is an array of $30\mu m \times 30\mu m$ square metallic columns of $h = 60\mu m$ high. The period of the structure is $a = 50\mu m$ and therefore the gap between to adjacent column is $20\mu m$. The structure is supposed to operate at $f = 1$THz and the beam size of a beam at this frequency is about $1cm$ and therefore the structure size should be few cm by few cm. In addition to that the conductivity of the metal is preferred to be as large as possible.

For fabrication of the device an area of $2cm \times 4cm$ is patterned using Deep Reactive-Ion Etching (DRIE) of silicon on a $3cm \times 5cm$ piece of silicon. After $60\mu m$ of etching, a $2\mu m$ thick layer of silver is sputtered on the patterned silicon. The skin depth of silver at $f = 1$THz is about $70nm$ and $2\mu m$ silver should be enough for preventing the fields to penetrate into the silicon. Fig. 5.2 show an image of the fabricated device.

Scanning electron microscope (SEM) images of this structure are shown in Figs. 5.3 and 5.4.

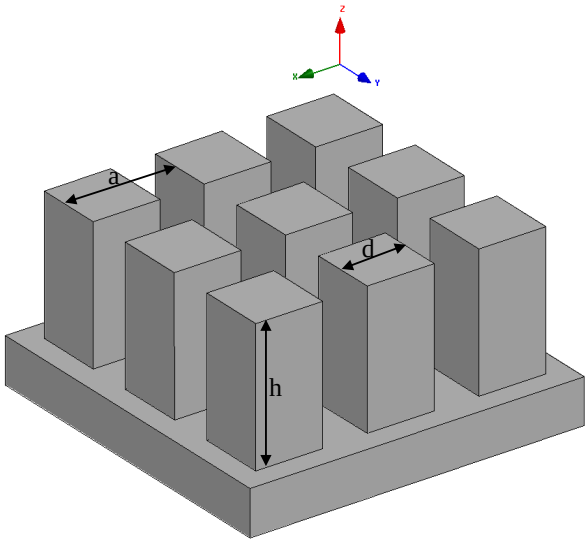

Figure 5.1: Proposed metallic periodic structure. The columns are $30\mu m \times 30\mu m \times 60\mu m$ ($d = 30\mu m$ and $h = 60\mu m$) and the period of the structure is $a = 50\mu m$.

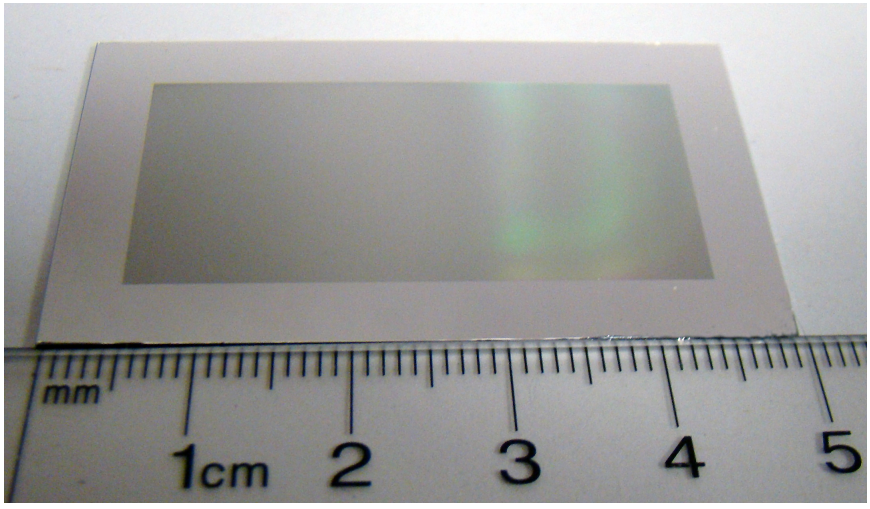

Figure 5.2: Image of the fabricated device.

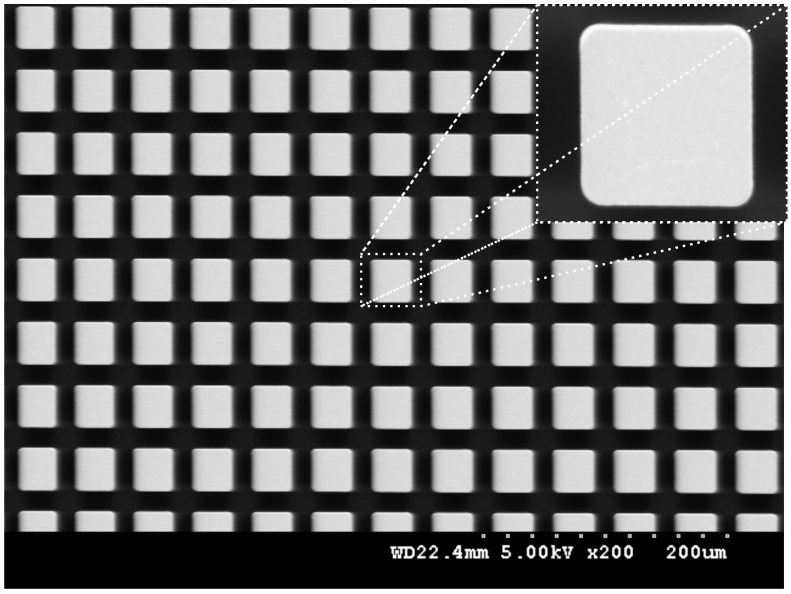

Figure 5.3: SEM image of the fabricated device (top view).

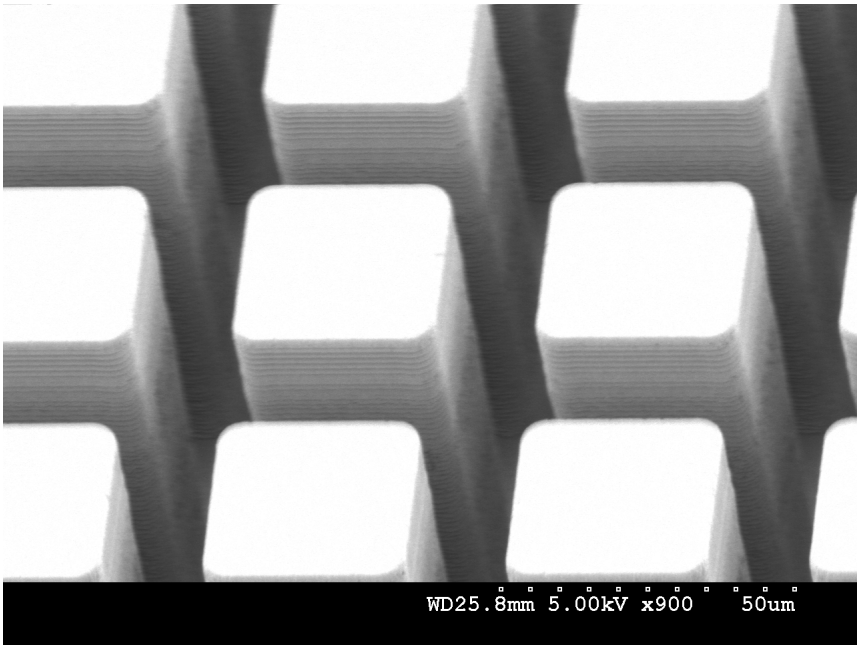

Figure 5.4: SEM image of the fabricated device (oblique view).

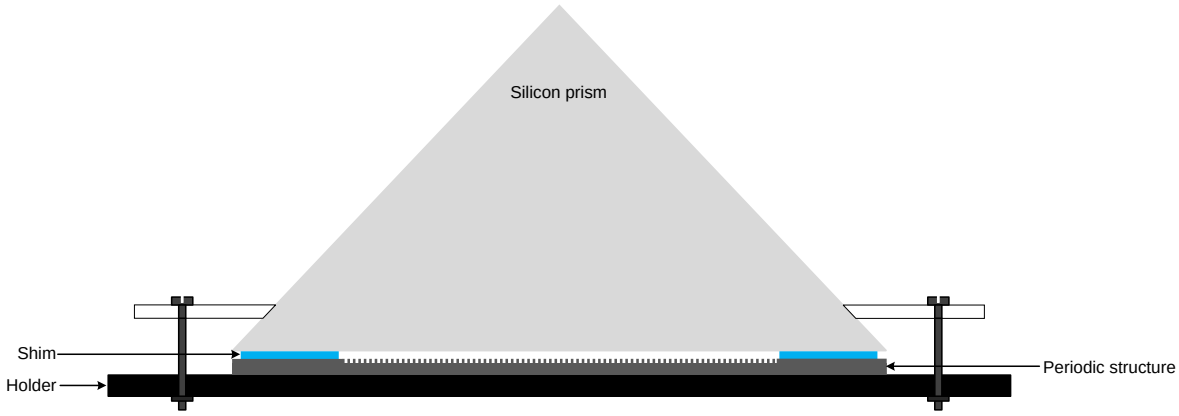

Figure 5.5: Schematic of the holders of the device and prism.

5.2 Experimental Setup

A measurement setup has been designed for coupling of continuos wave THz radiation into the surface waves propagating on the fabricated periodic structure.

As it is shown in Fig. 5.5, the fabricated structure is fixed on a holder and plastic shims with known thickness have been put on top of the unpatterned part to adjust the gap size. A silicon prism has been put on top of the shims. Another holder that pushes the prism down is tightened to the back holder by bolts and nuts. Fig. 5.6 shows an image of the prism and holders which is mounted with along with a THz mirror on a rotation stage.

The experimental setup is shown in Fig. 5.7 and its schematic in Fig. 5.8. Source of THz radiation is a Backward Wave Oscillator (BWO) which generates tens of milliwatts of continues wave millimeter-wave radiation and is tuneable in the frequency range of 87 to 180GHz. The output of BWO is frequency multiplied by diode multipliers to cover frequencies up to about 1.5THz. The THz wave radiated at end of the multipliers waveguide is polarized in the direction perpendicular to the optical table. A THz lens collects the radiated wave and its output is a collimated beam. For characterization of beam shape a pinhole has been scanned in a plane perpendicular to the beam axis and it has been found that at the frequency of $f = 1$THz a Gaussian beam with $W_0 = 6800\mu m$ is a good approximation for the THz beam.

The beam should enter the prism and after undergoing total internal reflection it should be detected by a THz detector. The measurement setup should be designed in a way that when the prism and the periodic structure is rotated to change the incident angle of the

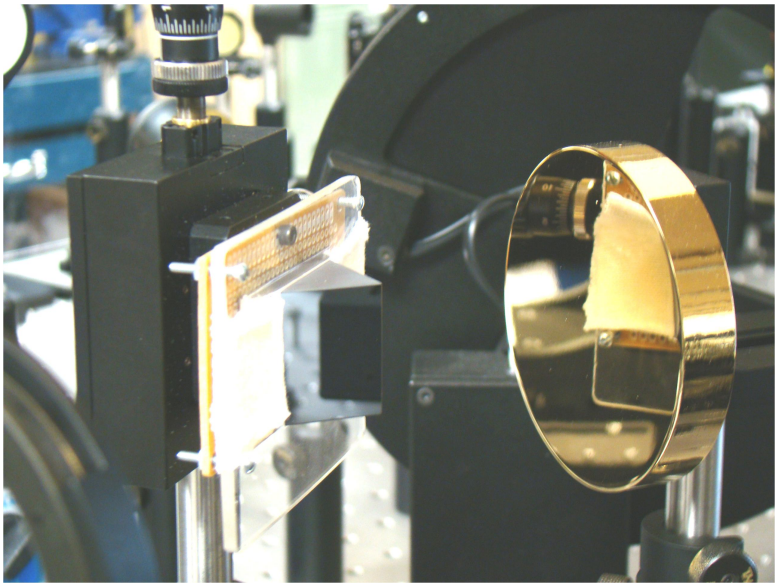

Figure 5.6: Image of the prism and holders.

beam, the beam should still go into the detector. This problem is become more clear if it be noticed that if a surface that the beam is reflected from is rotated by an angle θ the reflected beam will be rotated by 2θ with respect to its previous direction. For tackling this problem another mirror is mounted on same rotation stage that the prism is mounted. The beam is reflected from this mirror first and then enters the prism (see Fig. 5.8). By using geometrical optics, it can easily be shown that the beam exiting the prism will preserve its orientation and lateral position if the rotation center be chosen to be the intersection of the extension of mirror surface and the periodic structure surface.

The beam exiting the prism is being focused to a THz detector using another THz lens. Detector of the THz radiation that has been used is a Golay-cell which is a room temperature THz detector that is able to detect THz radiations with the tens of nanowatts of power. Measurement is currently being don by another member of group.

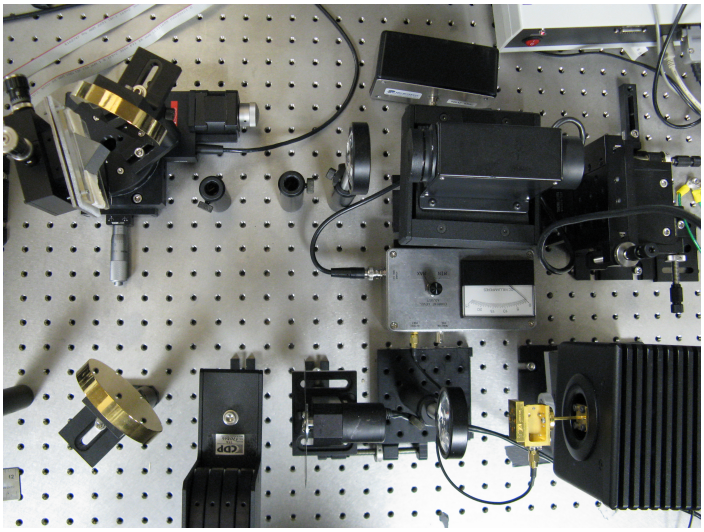

Figure 5.7: Image of the experimental setup.

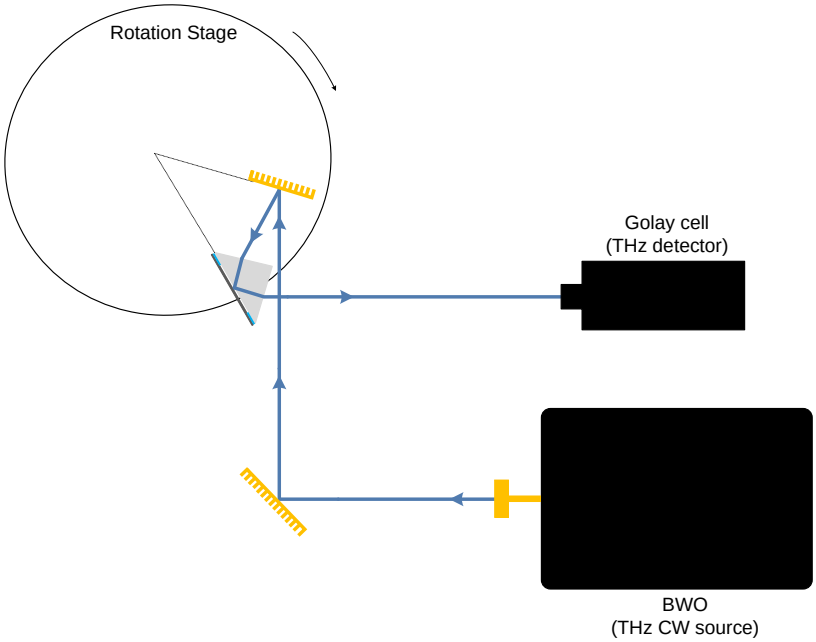

Figure 5.8: Schematic of experimental setup of Fig 5.7.

Chapter 6

Summary and Future Research

6.1 Summary

The extension of the idea of optical surface plasmon polaritons to THz frequencies was presented in this thesis. A review on the main properties of optical surface plasmon polaritons that propagate along a metal-dielectric interface was presented and it was discussed that negative real part of the permittivity of metals is responsible for existence of these waves. Typical methods for coupling of free propagating waves to surface plasmon polaritons were also presented. Existence and properties of THz surface plasmon polaritons on a metal-dielectric interface was demonstrated next and it was concluded that these waves are loosely bonded to the interface and cannot be used for making sensors. Doped semiconductors were also found to be too lossy to guide THz surface plasmon polaritons.

The possibility of guiding surface waves with field distribution similar to that of surface plasmon polaritons was considered in the chapter 3. A metallic two dimensional photonic crystal was proposed and it was shown that the proposed structure supports a surface wave that its propagation constant is very sensitive to the material near the surface of the structure. Otto's configuration was used for coupling of a TM beam to the surface wave. A sensitivity parameter was defined to quantify the performance of the sensor and using an analytical derivation, it was shown that the sensitivity is proportional to the time over which fields interact with the sample.

A novel method based on scattering parameter modeling of a cell of a periodic structure was introduced in chapter 4 to model the coupling of free propagating waves into surface waves. A method that uses eigen-frequency simulation of a single cell of the structure

for calculation of coupling parameters of a cell was demonstrated. The validity of the model was verified by full wave simulation of incidence of a plane wave and comparing its results with the results found from scattering parameter model. Incorporating the PWE method along with the scattering parameter model for coupling, coupling of a Gaussian beam to the surface waves was simulated. Local plane wave approximation method was also introduced and it was shown that provided the condition for its validity be satisfied, it gives accurate results and has the advantage that can be used for simulation of coupling of waves to aperiodic structures as well.

Fabrication and characterization of the proposed structure were presented in chapter 5. The details of the experimental setup which was designed for coupling of a THz beam to the fabricated structure were explained as well.

6.2 Future Research

It should be noted that the research work presented in this thesis for designing a sensor based on THz surface plasmon polaritons was mostly proof of concept and more sophisticated devices and configurations can be devised. Other methods of coupling of waves to the surface waves can also be investigated. Another line of research can be integration of surface plasmon polariton based sensors with a THz photomixing based source or a quantum cascade laser. Alternative fabrication techniques may also be used to decrease the fabrication cost.

References

[1] A. Arbabi, A. Rohani, D. Saeedkia, and S. Safavi-Naeini. A terahertz plasmonic metamaterial structure for near-field sensing applications. *Proceedings of 33rd International Conference on Infrared, Millimeter and Terahertz Waves*, 2008. 2

[2] W. L. Barnes, A. Dereux, and T. W. Ebbesen. Surface plasmon subwavelength optics. *Nature (London)*, 424:824–830, 2003. 2

[3] R. E. Collin. *Field theory of guided waves.* IEEE Press, 2nd edition, 1990. 2, 14, 15

[4] M. V. Exter and D. Grischkowsky. Optical and electronic properties of doped silicon from 0.1 to 2 thz. *App. Phys. Lett.*, 56(17):1694–1696, April 1990. 14

[5] R. F. Harrington. *Time Harmonic Electromagnetic Fields.* McGraw-Hill, New York, 1961. 2, 15

[6] A. P. Hibbins, B. R. Evans, and J. R. Sambles. Experimental verification of designer surface plasmons. *Science*, 308:670–672, April 2005. 2, 14

[7] J. Homola, editor. *Surface Plasmon Resonance Based Sensors.* Springer, 2006. 2, 5, 6

[8] J. Homola, S. S. Yee, and G. Gauglitz. Surface plasmon resonance sensors: review. *Sensors and Actuators B*, 54(1-2):3–15, Jan. 1999. 2

[9] N. Katzenellenbogen and Grischkowsky. Electrical characterization to 4 thz of n- and p-type gaas using thz time-domainspectroscopy. *App. Phys. Lett.*, 61(7):840–842, Aug. 1992. 14

[10] E Kretschmann and H. Raether. Surface plasmon resonance. *Z Naturforsch*, page 21352136, 1968. 2

[11] Matthew J. Lockyear, Alastair P. Hibbins, and J. Roy Sambles. Microwave surface-plasmon-like modes on thin metamaterials. *Phys. Rev. Lett.*, 102, Feb. 2009. 2

[12] S.A. Maier, S. R. Andrews, L. Martin-Moreno, and F. J. Garcia-Vidal. Terahertz surface plasmon polariton propagation and focusing on periodically corrugated metal wires. *arxiv*, 2006. 2, 14

[13] Stefan A. Maier. *Plasmonics: Fundamentals and Applications*. Springer, 2007. 2

[14] F. Miyamaru, S. Hayashi, C. Otani, and K. Kawase. Terahertz surface-wave resonant sensor with a metal hole array. *Optics Lett.*, 31(8):1118–1120, April 2006. 2

[15] M. A. Ordal, R. J. Bell, R. W. Alexander, L. L. Long, and M. R.Querry. Optical properties of au, ni, and pb at submillimeter wavelengths. *App. Optics*, 26(4):744–752, Feb. 1987. 11

[16] M. A. Ordal, R. J. Bell, R. W. Alexander, L. A. Newquist, and M.R. Querry. Optical properties of al, fe, ti, ta, w, and mo at submillimeter wavelengths. *App. Optics*, 27(6):1203–1209, March 1988. 11

[17] M. A. Ordal, Robert J. Bell, R. W. Alexander, L. L. Long, and M.R. Querry. Optical properties of fourteen metals in the infrared and far infrared:al, co, cu, au, fe, pb, mo, ni, pd, pt, ag, ti, v, and w. *App. Optics*, 24(24):4493–4499, Dec. 1985. 11, 12

[18] M. A. Ordal, L. L. Long, R. J. Bell, S. E. Bell, R. R. Belland R. W. Alexander, and C. A. Ward. Optical properties of the metals al, co, cu, au, fe, pb, ni, pd,pt, ag,ti, and w in the infrared and far infrared. *App. Optics*, 22(7):1099–1120, April 1983. 11

[19] A. Otto. Excitation of nonradiative surface plasma waves in silver by the methodof frustrated total reflection. *Zeits. Phys.*, 216:398, 1968. 2

[20] J. B. Pendry, L. Martin-Moreno, and F. J. Garcia-Vidal. Mimicking surface plasmons with structured surfaces. *Science*, 305:847–848, August 2004. 2, 15

[21] Bahaa E. A. Saleh and Malvin Carl Teich. *Fundamentals of Photonics*. Wiley-Interscience, 2nd edition, 2007. 33, 40, 41

[22] K. Wang and D. M. Mittleman. Metal wires for terahertz wave guiding. *Nature (London)*, 432:376–379, 2004. 2, 13

[23] C. R. Williams, S. R. Andrews, A. I. Fernndez-Domnguez, L. Martn-Moreno, S. A. Maier, and F. J. Garca-Vidal. Highly confined guiding of terahertz surface plasmon polaritons on structured metal surfaces. *Nature Photonics*, 2(3):175–179, March 2008. 2